Efficient coupling of tapered optical fibers to silicon nanophotonic waveguides on rare-earth doped crystals

Thesis by
Yan Qi Huan

In Partial Fulfillment of the Requirements for the
Degree of
Bachelor of Science in Physics

CALIFORNIA INSTITUTE OF TECHNOLOGY
Pasadena, California

2019
Defended May 20, 2019

Yan Qi Huan
ORCID: 0000-0002-6505-7150

ACKNOWLEDGEMENTS

First and foremost, I would like to thank Professor Andrei Faraon, my thesis advisor, for giving me a chance to work in his group during my search for a SURF last year, which led naturally to the starting of this project. Working with you and in your lab, has certainly shaped and consolidated my interest in various aspects of quantum physics. If it weren't for working in this lab, I'm sure I would have had a very different senior year, and probably a very different next 6+ years in a different graduate school. Thanks for you for the incisive comments and support on my work, your enthusiasm about both science and everything else, and for your advice on future career paths.

Equally importantly, I would like to thank Jake for everything over this past year. For teaching me from scratch about every single step of the project, for staying with me in the cleanroom into the evenings to finish the fab work, for always checking in with me to to see if I have enough resources to work efficiently, and for always being available to answer my silly questions and ideas. I really appreciate the amount of time you spent working with me, and I hope that you had enough time to spend on your own work as well (and hopefully equipment stop breaking!).

I am greatly thankful to everyone else in Faraon group as well. One year of working here has certainly flown by in the blink of an eye. In particular, thank you to Jon for giving me such a good introduction to the field of rare-earths when I joined the group a year ago for my SURF project and inspiring me to continue working in this area. Thanks to John, for providing me with advice on everything in the lab I could ever hope to know about. I wish you both the best of luck in your upcoming appointments. Thanks to Andrei R. and Greg for your warm welcomes and companionship when I suddenly arrived in your office one fine Monday last summer. Thanks to Ioana for your energy, enthusiasm, and for letting me borrow your setup for a few weeks. To everyone else in the group, while I may not have had the opportunity to interact with you as much during my time here, I still enjoyed everyone's presence for creating such a friendly group atmosphere. I look forward to crossing paths with everyone in the future.

Thank you to the various processors who contributed to my undergraduate experience, especially Professors Rob Phillips and Dave Stevenson, for organizing Ph 11. It was an invaluable community for me, a bumbling freshman, to get in touch with

several other like-minded students and to think about research in more than one way. Thanks to my friends, in particular Tong for keeping in touch over the past couple of years despite being half the globe away, and for being such a good listening ear when we were ranting to each other about our respective projects.

And of course, as always, thank you to my brother and parents for all their support and help that they have given me all this time.

ABSTRACT

Quantum networks are a rapidly developing field of quantum information processing that have the potential to enable long-range entanglement between future quantum computers as well as the implementation of secure communication through quantum key distribution. Two key components of such networks are quantum memories to store entangled photon pairs for use in the quantum repeater protocol and quantum light-matter interfaces to efficiently interconvert between stationary qubits and flying qubits in the form of photons. Rare-earth ion-doped crystals are a promising solid-state platform that show promise for both of these applications due to their long optical and spin coherence times. Due to their relatively weak optical transitions, rare-earth ions have been coupled with nanophotonic resonators to enhance their transition strengths, with past work in the Faraon group utilizing focused ion beam milled photonic crystal resonators with 45° angled couplers to couple light in and out. Such resonators have the disadvantage of requiring manual alignment to fabricate, and the couplers are also relatively inefficient which limits the performance of such devices. It is therefore desirable to move towards silicon photonics, where mature techniques such as electron-beam lithography can allow for scalable fabrication of nanophotonic cavities together with high coupling efficiencies.

In this thesis, we demonstrate significant progress towards the usage of acid-etched tapered optical fibers as an efficient interface for coupling light into tapered silicon nanophotonic waveguides. We show comprehensive simulations of the taper geometries required to achieve adiabatic coupling with theoretical efficiencies of more than 99%, and design a silicon photonic crystal mirror to be used in the measurement of the fiber-waveguide coupling efficiency. We then optimize the hydrofluoric acid fiber etching process and demonstrate the ability to make tapered fibers which are 200 µm long with a taper half-angle of 2° and a tip diameter of 50 nm. Using these tapered fibers to couple light into tapered silicon waveguides fabricated using electron-beam lithography shows a moderately high coupling efficiency of 11.4% with the potential for improvement. This method of tapered fiber coupling shows promise to be integrated into silicon nanophotonic resonators on rare-earth ion doped crystals and allow for highly efficient quantum memories and quantum light-matter interfaces in the solid-state.

TABLE OF CONTENTS

LIST OF ILLUSTRATIONS

LIST OF TABLES

Chapter 1

INTRODUCTION

1.1 Quantum networks and nodes

Quantum computing is currently experiencing an age of rapid growth, with large amounts of interest and capital invested by governments as well as companies such as Google [1], IBM Q [2], IonQ [3], and many more others. The goal of these efforts is, of course, to build a scalable universal fault-tolerant quantum computer that can potentially leverage on the properties of superposition and entanglement of quantum systems to implement algorithms that are not possible in classical physics. From this, the goal is to achieve quantum supremacy [4], whereby the quantum computer can perform calculations that are intractable for classical computers.

Some potential problems that are classically difficult but might be feasible on quantum computers include integer factoring, for which Shor's algorithm [5] has an exponential speedup over the best-known classical algorithm, particle physics simulations [6], as well as quantum simulation of molecular energies levels [7].

At the same time, while quantum computing receives most of the media headlines and coverage, quantum communication and networking is another important subfield of quantum information processing which complements quantum computing and allows future quantum computers to maximize their usage and potential. Put simply, quantum networks consist of local quantum nodes connected via quantum channels that can transmit quantum information coherently. This potential "quantum internet" [8] (Fig. 1.1), which can be viewed as an analog to the classical internet, could allow secure communication and transfer of quantum entanglement information between future quantum computers. By sharing entanglement between quantum computers, we can overcome technological limitations on the scale of a single computer by making multiple nodes communicate and share quantum information with each other to work on a computation in tandem.

Furthermore, having access to quantum channels between distributed users gives rise to the possibility of quantum cryptography [10], where one can leverage the inherent randomness of quantum mechanics to achieve provably secure communications even involving untrusted partners. One particular application is in quantum key distribution [11, 12], in which two parties can securely share a secret key for

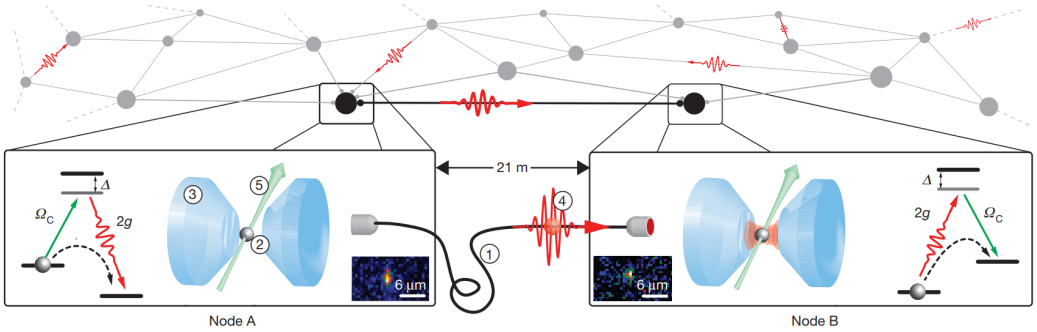

Figure 1.1: Schematic of a quantum network connecting two nodes (represented by atom traps) with an optical fiber carrying a photon with the quantum information. The background shows a possible network consisting of numerous nodes and quantum channels. Image from [9].

encrypted communications and can detect the interference of any eavesdropper trying to intercept the key.

In terms of physical implementation, optical quantum networks can be implemented simply as optical fibers that connect the quantum nodes of interest. If the qubits on two ends are located on solid-state platforms, another crucial ingredient would then be quantum light-matter interfaces (QLMIs), which are devices that coherently and reversibly couple quantum information from stationary qubits to photons that are used as "flying qubits" to be sent through the fiber to establishment entanglement with the remote quantum node[8]. On the receiving end, another QLMI would then convert the photon back into a stationary qubit while maintaining the stored quantum information. Photons are ideal carriers of quantum information since they can travel over long distances with low interaction cross-sections and thus can hold onto their quantum information for a long time. Moreover, optical photons in particular are desirable as optical fibers can be made with extremely low losses of less than $0.2\,\mathrm{dBkm}^{-1}$ in the 1550 nm band [13], and they are robust against thermal excitations even at room temperature compared to microwave photons.

However, even with the current excellent state of optical fiber technology, a photon traveling for 500 km would experience an attenuation of 100 dB, which means that it would almost certainly be lost and not reach the other end. Thus, an additional piece of infrastructure, known as quantum repeaters [14], is necessary for long-distance communications spanning large parts of a country or continent. Such a scheme works by storing entangled pairs at various intermediate nodes along the actual quantum channel, where the distance between these nodes are short enough

that a fiber can travel between them with high efficiency. Repeated applications of entanglement swapping between the pairs of entangled particles allows for the two endpoints to eventually share an entangled Bell pair, even though the distance between them is too large for any single photon to have traveled all the way between them. This Bell pair can then be used to transmit quantum information through quantum teleportation.

As part of this scheme, an indispensable component is a quantum memory that can store quantum states which we can read-out on demand, since the entanglement swapping process is probabilistic and thus the photon from each Bell pair will need to be held in memory for some time while it waits for its counterpart to prepared before they can be measured in the Bell basis for the entanglement swapping.

As we will see in the next section, it turns out that rare-earth ions (REIs) in solids are a highly promising potential platform for the implementation of both QLMIs and quantum memories. While we will be focusing on REIs in this thesis, the interested reader may refer to [15] for a review on various solid-state systems that have optical interfaces as potential QLMIs, while Heshami et al [16] has a comprehensive review of quantum memories and their implementation on various other platforms.

1.2 Rare-earth ions for quantum information applications

There are several reasons why REIs in solids have presented themselves as an attractive option for such applications in quantum information processing. Firstly, as it is a solid-state system, it is much easier to fabricate all the components on-chip, making miniaturization and scaling up potentially easier to accomplish. More importantly, they have demonstrated excellent coherence times of up to several milliseconds for the optical transition in Er^{3+}:Y_2SiO_5 [17] and up to 6 hours in the spin transition of Eu^{3+}:Y_2SiO_5 [18]. This allows us to use them for long-lived storage as quantum memories as well as high fidelity qubits where many gates can be done on the quantum state before decoherence occurs.

Additionally, certain isotopes of REIs, such as $^{167}Er^{3+}$ and $^{171}Yb^{3+}$, have nonzero nuclear spin which gives rise to long-lived spin states arising from the hyperfine interaction and can potentially be used for spin-wave storage [19]. At the same time, these two elements are also Kramers ions by virtue of them having an odd number of electrons [20], meaning that they have a strong magnetic dipole moment on the order of μ_B and thus we can rapidly manipulate their quantum state using microwave pulses. The presence of microwave transitions together with optical transitions also

opens the possibility of microwave-to-optical transduction applications [21] so that superconducting qubits, which operate in the microwave regime, may be coupled with optical photons and transmit their quantum information over long distances.

Finally, Er^{3+}:Y_2SiO_5 in particular has attracted a lot of attention as the $^4I_{15/2} \leftrightarrow {}^4I_{13/2}$ transition in this system has a wavelength of 1536 nm [17] which lies right within the window of minimum loss of optical fibers [13] used for long-haul optical transmission systems. Therefore, this system has the potential to be used to directly couple light into low-loss optical fibers for long-distance quantum communications without the need for frequency conversion.

1.3 Nanophotonic coupling interfaces

While REIs do indeed have long optical coherence times, the flip side is that they have weak $4f$-$4f$ optical transitions as these transitions are supposed to be forbidden by selection rules but only partially allowed by crystal field mixing [22], leading to slow operation times and lower pumping efficiencies. In order to enhance the optical transition strength, the REIs can be integrated into optical cavities resonant with the transition frequency, and the spontaneous emission rate would be enhanced by the Purcell effect by a factor inversely proportional to the cavity's mode volume [23].

In the Faraon lab, photonic crystal cavities have been realized in numerous REI systems, such as Nd^{3+}:Y_2SiO_5 (Nd:YSO) [24], Nd^{3+}:YVO_4 (Nd:YVO) [25], Er^{3+}:YSO [26], and Yb^{3+}:YVO [22], in order to enhance the optical transition strengths and efficiently optically access the ions resonant with the cavity. Recently, the usage of such nanophotonic cavities have enabled the addressing and control of single Nd^{3+} ions and Yb^{3+} in YVO [22, 27], indicating promising results for applications in future quantum networks.

For these demonstrations of cavity enhancement of the optical transition, the optical cavity was directly fabricated onto the surface of the YSO or YVO crystal using focused ion beam (FIB) milling to form a photonic crystal resonator [28, 29] as shown in Fig. 1.2. Laser pulses are sent into the cavity and emitted photons from the cavity are received through a 45°-angled coupler that is located at the ends of the cavity (shown in the dotted red square of Fig. 1.2). Incoming laser light is focused using an aspheric doublet directly onto the coupler, and past experiments have demonstrated relatively low efficiencies of 20% to 30% [24, 27]. A low coupling efficiency limits the percentage of photons emitted from the REIs in the

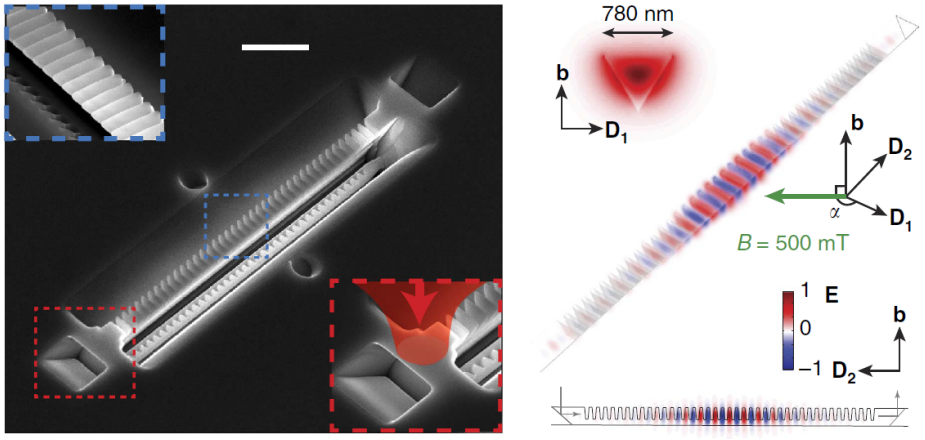

Figure 1.2: Photonic crystal triangular nanobeam resonator fabricated in Nd:YSO using focused ion beam milling . Image from [24].

cavity that can be collected, which correspondingly limits the maximum efficiency of any QLMIs or quantum memories in these platforms.

At the same time, another disadvantage of this FIB fabrication process is that it is time-consuming and requires manual alignment. This suggests that we should move towards more automated and repeatable fabrication techniques such as electron-beam lithography. However, this technique is not compatible with YSO and YVO, and we would need to deposit a layer of material such as silicon on top of the substrate before we can use electron-beam lithography to pattern photonic crystals onto the silicon waveguide. The REIs within the YSO/YVO substrate would then be indirectly coupled to the optical power in the waveguide through evanescent coupling.

As such, it is beneficial for us to investigate more efficient methods of coupling laser light from optical fibers to the silicon nanophotonic waveguides that we will be depositing on top of the REI-doped crystal. Several methods for doing this have been explored, including grating couplers [30], end-fire coupling [31], and heat-and-pull tapering of the optical fiber leading to biconical tapered fiber geometry [32] and single-sided tapered fibers [33]. However, grating couplers require relatively complex surface geometry etching to achieve a high efficiency [30] and have a fixed diffraction angle which makes alignment of the fiber sensitive, while end-fire coupling require that the couplers must be located at the edge of the chip [34]. On the other hand, although fiber pulling methods have achieved efficiencies of 97% [33], they are complicated experimentally since they require the fiber to be heated using a flame while the fiber is pulled from both ends at a precise rate to achieve the

desired fiber profile.

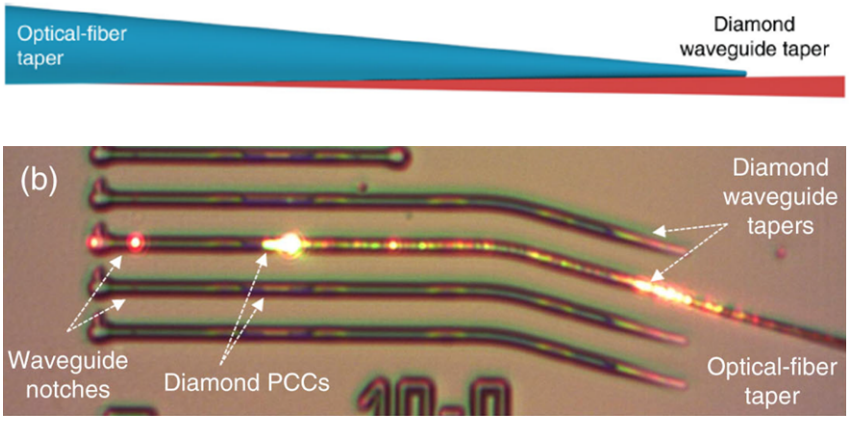

Figure 1.3: Optical fiber taper coupling with diamond waveguide taper. Image from [35].

Instead, we choose to use a wet-etching method using hydrofluoric acid (HF) [36] to create an optical fiber with variable taper geometry for our purposes. This method has been used in diamond nanophotonic waveguides to achieve coupling efficiencies in excess of 95% [35], and a schematic of the coupling interface as well as an experimental image is shown in Fig. 1.3. Additionally, it is considerably simpler to implement compared to the heat-and-pull method since it only requires dipping the fiber in a HF solution and moving the fiber vertically at a given speed.

In our case, we will aim to replicate the same coupling method but with a tapered silicon waveguide instead of a diamond waveguide. The silicon waveguide will be tapered along the region of overlap with the tapered fiber in order to adiabatically change the effective mode index from that of the fiber to that of the silicon to achieve maximum transmittance and minimal reflection or scattering.

However, unlike Burek et al. [35] who etched the waveguide directly into their diamond substrate, our usage of a silicon intermediate layer on top of a YSO/YVO substrate presents additional difficulties. This is because when the index of the material under the silicon (1.8 for YSO) is greater than that of the fiber (1.45), the incoming light can couple to the radiation modes of the substrate, causing a greatly reduced coupling efficiency into the silicon waveguide. To solve this problem, we propose elevating the silicon taper and thus creating an air gap below it in the fiber coupling region. However, the actual fabrication of this elevated silicon waveguide "bridge" is outside the scope of this project, and we will only focus on the fiber fabrication and the testing of the coupling interface.

1.4 Overview of thesis

In this thesis, our aim is to apply the meniscus etching technique to fabricate tapered fibers and maximize optical coupling efficiencies with a silicon nanophotonic waveguide structure.

A schematic of our desired experimental geometry is shown in Fig. 1.4. The figure shows the three main components of our fiber-waveguide coupling interface – an optical fiber tapered from left to right, a silicon waveguide tapered from right to left, and a photonic crystal mirror patterned into the waveguide to reflect light back into the fiber in order to measure the reflected power and estimate the coupling efficiency.

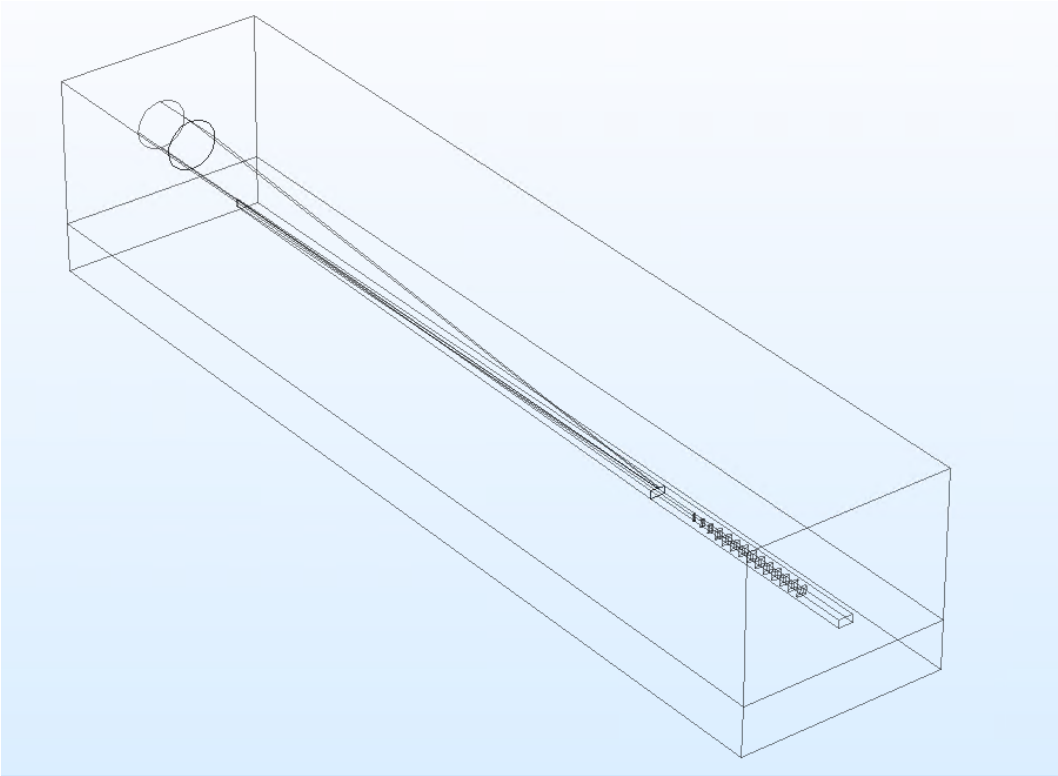

Figure 1.4: Schematic of overall fiber-waveguide coupling setup, with the fiber tapering from left to right, the waveguide tapering from right to left , and a photonic crystal mirror on the right portion of the waveguide.

This thesis presents significant progress towards the practical usage of tapered fibers as a high-efficiency interface between optical fibers and silicon nanophotonics. We provide detailed simulations across a range of geometrical parameters of the components to optimize for the coupling efficiency, and proceed to optimize fabrication techniques to achieve the design geometry from simulations. We then combine these

components together to perform coupling efficiency measurements and demonstrate indications of successful coupling with an preliminary efficiencies of 11.4%.

This first chapter has provided an overview on the potential applications of rare-earth doped crystals as a potential platform for quantum information and communication applications, and motivates the need for an improved method of coupling into the nanophotonic waveguides in these systems to improve device efficiency.

Chapter 2 provides a brief theoretical background on the various aspects of the tapered fiber system as a nanophotonic coupling platform, starting with a review of electromagnetic wave theory to understand the requirements for high transmission at an interface between two media. We also study photonic crystals and how they create a band gap and reflect light so as to allow us to measure the coupling efficiency at the fiber-waveguide interface. Finally, we take a detailed look at the physical mechanism behind how HF can create a tapered tip on an optical fiber.

Next, chapter 3 goes into detail about the finite-element simulations to determine the mode indices and transmittance between tapered fibers and waveguide as a function of the taper geometry and relative positions of the fiber and waveguide. Simulation results that determine the dimensions of a photonic crystal that shows a sizable reflection at the target wavelength are also presented. Together, these simulation results provide a target design for the fabrication process.

Chapter 4 provides an outline on the experimental setup and procedures used for the fiber acid etching, waveguide fabrication, and the coupling measurements between the fiber and the waveguide. The results of the fabrication process and the coupling measurements are then presented and discussed in chapter 5.

Finally, we conclude the thesis in chapter 6 with a discussion of our progress towards efficient tapered-fiber coupling and improvements that can be made for this become a convenient coupling mechanism in future rare-earth ion devices.

Chapter 2

THEORETICAL BACKGROUND

In this chapter, I will describe the theoretical foundations of the various tools and procedures that were used in both our simulations and experimental procedures and design. The first section will give an overview of the theory of electromagnetic (EM) waves and light propagation, since the experimental focus of this thesis is to optimize the coupling of light from one medium into another. Following this, I will give a brief introduction to the theory of photonic crystals. Even though they are not a key component of the actual coupling interface between the tapered fiber and the optical fiber, they are important in allowing us to simplify the experimental measurements of the interface coupling efficiencies. Finally, I will discuss the theory behind the procedure of etching optical fibers using acid and how tapers are formed.

2.1 Electromagnetic wave theory

Wave equation

In order to analyze the transmission of light through the fiber-waveguide interface, a natural place to start would be from the wave equation of light. This can easily be derived from the Maxwell's equations, which are [37]:

$$\nabla \cdot \mathbf{B} = 0 \qquad \nabla \times \mathbf{E} + \frac{\partial \mathbf{B}}{\partial t} = 0 \tag{2.1}$$

$$\nabla \cdot \mathbf{D} = \rho \qquad \nabla \times \mathbf{H} - \frac{\partial \mathbf{D}}{\partial t} = \mathbf{J} \tag{2.2}$$

Here, the charge density ρ and the current density $\mathbf{J}$ refer to the free charge densities. In all cases that we are considering, there will be no free charges and currents in the system, and thus they can be set to zero.

In the case of a linear material, we have the linear constitutive relations:

$$\mathbf{D} = \varepsilon_0 \varepsilon(\mathbf{r}) \mathbf{E} \tag{2.3}$$

$$\mathbf{B} = \mu_0 \mu(\mathbf{r}) \mathbf{H} \tag{2.4}$$

where ε and μ are the relative permittivities and the relative permeabilities respectively. They are functions of position since we would like to consider interfaces

between different materials which have different field responses. We assume that this position dependence only takes the form of step functions, i.e. all materials are internally homogeneous and the boundaries between different materials is sharp. This is because the fiber and silicon waveguides have homogeneous permittivities, and we only aim to shape their geometry but not their material properties. Additionally, we make the additional assumption that $\mu(\mathbf{r}) = 1$ everywhere, since all of the materials under consideration are non-ferromagnetic and have very weak magnetic responses.

Substituting these constitutive relations into the Maxwell's equations with no free sources, we get:

$$\nabla \cdot \mathbf{H} = 0 \qquad \nabla \times \mathbf{E} + \mu_0 \frac{\partial \mathbf{H}}{\partial t} = 0 \tag{2.5}$$

$$\nabla \cdot (\varepsilon(\mathbf{r})\mathbf{E}) = 0 \qquad \nabla \times \mathbf{H} - \varepsilon_0 \varepsilon(\mathbf{r}) \frac{\partial \mathbf{E}}{\partial t} = 0 \tag{2.6}$$

where the electric and magnetic fields are implicitly functions of $\mathbf{r}$ and t as well.

From here, for each of the curl equations, we can take their curl and simplify using the other curl equation:

$$\nabla \times \left(\frac{1}{\varepsilon(\mathbf{r})} \nabla \times \mathbf{H} \right) = -\mu_0 \varepsilon_0 \frac{\partial^2 \mathbf{H}}{\partial t^2} \tag{2.7}$$

$$\nabla \times (\nabla \times \mathbf{E}) = -\mu_0 \varepsilon_0 \varepsilon(\mathbf{r}) \frac{\partial^2 \mathbf{E}}{\partial t^2} \tag{2.8}$$

Finally, in order to decompose any electromagnetic wave into its constituent normal modes whose values vary sinusoidally in time, we split each component into a separable products of its spatial and time part:

$$\mathbf{E}(\mathbf{r}, t) = \mathbf{E}(\mathbf{r}) e^{-i\omega t} \tag{2.9}$$

$$\mathbf{H}(\mathbf{r}, t) = \mathbf{H}(\mathbf{r}) e^{-i\omega t} \tag{2.10}$$

Plugging this into equations 2.7 and 2.8 gives us the wave equations, which we write down as equations 2.11 and 2.12.

$$\boxed{\nabla \times \left(\frac{1}{\varepsilon(\mathbf{r})} \nabla \times \mathbf{H} \right) = \frac{\omega^2}{c^2} \mathbf{H}} \tag{2.11}$$

$$\boxed{\nabla \times (\nabla \times \mathbf{E}) = \frac{\omega^2}{c^2} \varepsilon(\mathbf{r}) \mathbf{E}} \tag{2.12}$$

where the fields now only have the implicit arguments over space and we have made the substitution $c = \frac{1}{\sqrt{\mu_0 \varepsilon_0}}$. These equations can be considered as eigenvalue equations for $\mathbf{E}(\mathbf{r})$ and $\mathbf{H}(\mathbf{r})$, and they can be solved to obtain the eigenvalues ω, which represent the frequencies of possible modes within the system, and the eigenvectors, which are the magnetic and electric fields. We note that we only need to solve one of these equations, because we could obtain the field distribution of the other field by using the curl equations in 2.5 and 2.6, and then simplify the time derivatives using equations 2.9 and 2.10. More explicitly, the result of combining these two sets of equations are:

$$\mathbf{E} = \frac{i}{\varepsilon_0 \varepsilon(\mathbf{r}) \omega} \nabla \times \mathbf{H} \tag{2.13}$$

$$\mathbf{H} = \frac{1}{i \omega \mu_0} \nabla \times \mathbf{E} \tag{2.14}$$

which allows us to obtain the electric field after solving for the magnetic field or vice versa. In particular, the COMSOL Electromagnetic Waves Frequency Domain User Interface [38] that we use for solving this equation solves the electric field equation (Equation 2.12). For a given value of the eigenvalue ω, the simulation then outputs for each value of effective mode index (discussed below) the computed eigenmodes, which are the normal mode electric field distributions.

Often, we will also consider 2D systems in the x-y plane which we assume to extend infinitely in the z-direction. In these geometries, because of the continuous translational symmetry in z, we can further expand the spatial part of the fields into a plane wave along the z-direction and an arbitrary x-y function, where we have $\mathbf{E}(\mathbf{r}) = \mathbf{E}(x, y)e^{ikz}$ for some possibly complex constant k. For a given choice of z-wavenumber k, we can solve for the eigenvalue ω as part of the eigenvalue equation.

These values of k, which we call the wavenumbers or propagation constants (also denoted as β), serve as another index to label a particular eigenmode of the wave equation. A quantity that will often be useful is the effective mode index [39], defined as $n_{\text{eff}} = \frac{k}{2\pi/\lambda_0}$ where $\lambda_0 = \frac{2\pi c}{\omega}$ is the free space wavelength associated with the particular angular frequency ω. This effective mode index is dependent both on the frequency and the particular choice of mode, and is the analogous quantity to the refractive index of a material in classical ray optics. In particular, it is real if the mode is lossless and any positive imaginary component represents decay of the mode in the propagation direction.

The effective mode index is a useful heuristic quantity for us to judge whether a particular interface is likely to have high transmission or high reflection. In an analogous manner to classical optics, a discontinuity in mode index leads to some reflection at that boundary, while a slowly-varying mode index would lead to a high transmission through that region.

Adiabatic mode transition

To make this idea more quantitative, we can consider the adiabadicity criterion [33, 39], which is a guide to how fast our fibers and waveguides should be allowed to taper before we would expect significant power losses due to coupling from the fundamental mode, which the wave is originally in, to higher order modes. This condition is derived from the comparison between two relevant length scales: z_t, the taper length-scale which measures how fast the fiber or waveguide's transverse dimension shrinks as a function of the axial dimension, as well as z_b, the beat length between the the fundamental and second-lowest supported mode with the same symmetry [1].

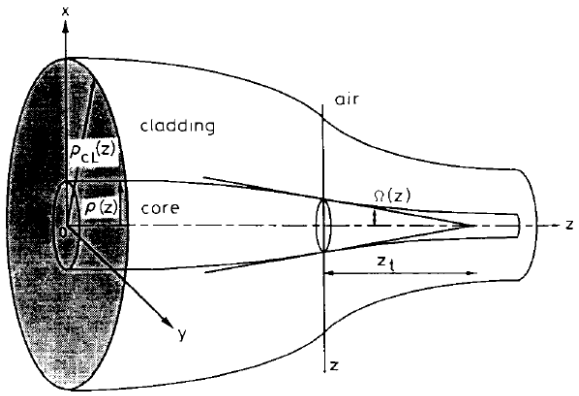

Figure 2.1: Schematic of a tapered fiber with relevant lengths labeled. Image from [39].

More specifically, let us define the taper length scale z_t as the axial length that would cause the fiber to shrink to a single point, assuming the local taper rate is extrapolated. For an illustration, we refer to Fig 2.1, which shows a tapered fiber with the taper length z_t labeled for a particular point. Here, $\Omega(z) \equiv \tan^{-1} |\frac{d\rho(z)}{dz}|$ is the local taper half-angle (half of the full cone angle), where z is the axial coordinate

[1] For instance, if the light is originally in the LP_{01} mode which has azimuthal symmetry, then the next highest mode that we should consider should be the LP_{02} mode even though other modes such as LP_{11} might have a smaller propagation constant.

and $\rho(z)$ is the fiber radius at a given point z. From this figure, we can therefore see that $z_t(z) = \frac{\rho(z)}{\tan\Omega(z)} \approx \frac{\rho(z)}{\Omega(z)}$ as most of our tapers have small enough angles to satisfy $\tan\Omega \approx \Omega$.

On the other hand, the beat length scale between the two nearest modes is given by $z_b(z) = \frac{2\pi}{\beta_0(z)-\beta_1(z)}$, where β_0 is propagation constant of the fundamental mode that the light starts out in and β_1 is the nearest feasible excited mode. Note that the propagation constants are indirect functions of z since they are functions of the local geometry, which is set by the radius $\rho(z)$. The adiabatic condition to prevent losses into higher-order modes is therefore the requirement that $z_t \gg z_b$, in other words:

$$\rho(z)/\Omega(z) \gg \frac{2\pi}{\beta_0(z) - \beta_1(z)} \tag{2.15}$$

Rearranging this, we can get a bound on the taper angle of the fiber and waveguides:

$$\Omega(z) \ll \frac{\rho(z)(\beta_0(z) - \beta_1(z))}{2\pi} \tag{2.16}$$

Burek et al [35] also present an alternative rewriting of this adiabatic condition in terms of the effective mode index.

$$\frac{dn_{wvg}}{dz} < \frac{2\pi}{\lambda}\left|n_{\text{eff},0}(z) - n_{\text{eff},1}(z)\right|^2 \tag{2.17}$$

where n_{wvg} is the waveguide effective index and λ is the free space wavelength.

2.2 Photonic crystals

In our setup for the measurement of the fiber-waveguide coupling efficiency, we require the presence of a mirror at the end of the waveguide in order to reflect the transmitted light back into the fiber. This is because we do not have a way of directly measuring the amount of light that has entered the waveguide on the chip, and instead it is more convenient to measure laser power when it is fiber-coupled by simply connecting it to a photodetector. Therefore, this necessitates the etching of photonic crystal holes in the waveguide to act as a mirror.

Here, we will only attempt to give a brief summary of only the important points that are relevant to our experimental design. For more details, one can refer to the comprehensive introduction to photonic crystals by Joannopoulos et al [37] which explains in depth the principles behind photonic crystal design and their applications.

Fundamentally, photonic crystal mirrors act by engineering the dispersion relation $\omega(k)$ of the medium such that there is a photonic band gap at the desired wave

frequency ω, meaning that there do not exist any supported modes at that given frequency.

Intuitively, one can understand how band gaps are formed by studying the simplest photonic crystal, a particular form of a multilayer film known as a quarter wave stack. This stack is formed by simply stacking alternating layers of two different materials in a stack in the z axis, as shown in Fig. 2.2. We assume that these layers extend infinitely in the x-y plane, and thus this system is effectively 1-dimensional. We consider sending light with a certain frequency ω and vacuum wavelength λ_0 at normal incidence, and set each layer's thickness to be $d = \lambda/4 = \lambda_0/(4n)$ where λ is the wavelength in that material and n is its refractive index. From this, we can simply apply classical relations for wave reflection and transmittance coefficients [40] at each interface where the impedance changes to obtain the overall reflectance of the entire stack. For the case where we have $2N + 1$ layers and when the quarter wave stack is placed in air, the reflectance of the stack can be computed using matrix optics to be [40]:

$$R = \frac{1 - \left(\frac{n_H}{n_L}\right)^{2N} n_H^2}{1 + \left(\frac{n_H}{n_L}\right)^{2N} n_H^2}$$

where n_H is the refractive index of the material with the higher index and n_L is the refractive index of the lower-index material, which means that $\frac{n_H}{n_L} > 1$. Therefore, for $N \to \infty$, we will get $R \to -1$, giving us a perfect mirror (the negative sign comes from the π phase shift when reflecting off an interface with higher impedance) for this quarter wave stack purely from simple wave mechanics considerations. Additionally, the reflectance converges to towards perfect reflection more rapidly when n_H/n_L has larger, i.e. the layers have a larger index contrast.

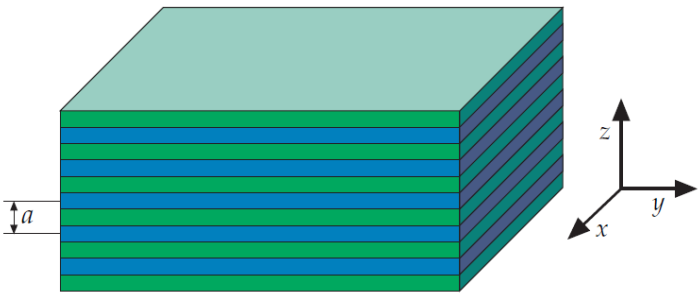

Figure 2.2: Schematic of a quarter wave stack, which is the simplest 1D photonic crystal. The different colors represent materials with different dielectric constants. Image from [37]

In the general case, we want to analyze the response of this system for wavelengths other than λ_0 and for different thicknesses of the layers. We do this by first making the approximation that this multilayer film continues periodically forever, and thus we do not need to be concerned with the surrounding medium and can simply apply a periodic boundary condition. From there, we can then solve the wave equation for the eigenfrequencies of the system as a function of the wave vector k, which corresponds to varying the wavelength of the incoming light, and then plot the set of allowed ω against k. One small change in this case is that we restrict the range of wave numbers k to lie within $[-\pi/a, \pi/a]$, where a is the sum of the thickness of each pair of adjacent layers. This is because our system has a discrete translational symmetry of period a along the z-axis, and thus adding $2\pi/a$ to any value of k will not make a difference to the system as it only contributes a phase of $(2\pi/a)(a) = 2\pi$ over the period a, which has no physical effect. Therefore, we typically scale our wave vectors to get a normalized wave vector $\tilde{k} = ka/2\pi$ such that it lies within the range $[-0.5, 0.5]$.

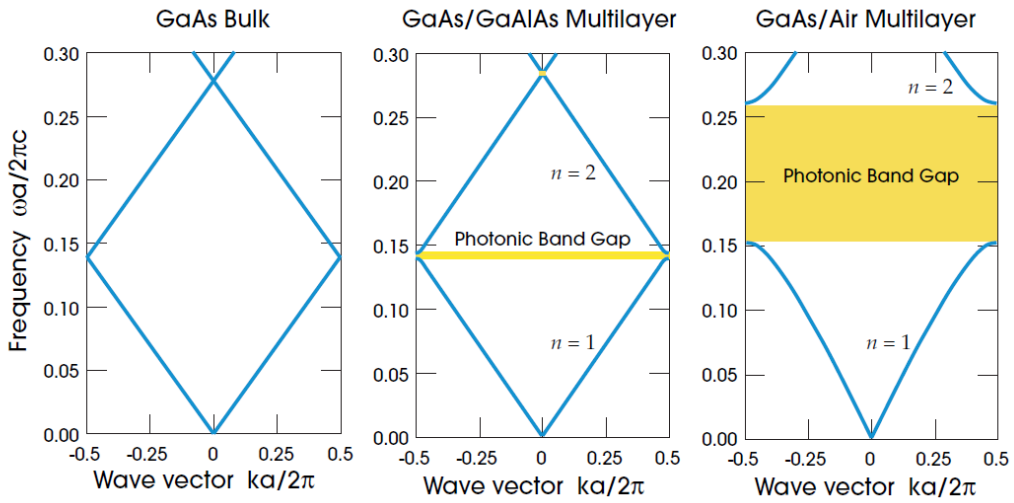

Figure 2.3: Typical band gaps for multilayer films with different refractive index contrast between the two materials. Image from [37].

The numerically computed band structures for various ratios of n_H/n_L is shown in Fig. 2.3, where the leftmost figure has $n_H/n_L = 1$, the middle figure has $n_H/n_L = 13/12$, and the rightmost figure has $n_H/n_L = 13$. Each layer of the film is set to have thickness $0.5a$. We make two key observations. Firstly, this is consistent with the direct computation of the reflectance earlier, where we saw that there is a perfect reflectance when each layer has thickness equal to $\lambda/4$. Applying the fact

that each layer has thickness $a/2$ and $\lambda = 2\pi/k$, we get that the perfect reflectance occurs at $\tilde{k} = ka/2\pi = 1/2$, which corresponds to the left and right edges of the dispersion relation plot where the band gap first opens up which leads to no transmission. Secondly, the size of the band gap increases as we increase the index contrast between the two layers, which also agrees with our previous observation that a greater index contrast gives rise to a higher reflectivity.

In our experimental setup, we have a similar geometry where we have a rectangular silicon waveguide with elliptical holes patterned into it (Fig. 2.4). Looking down the length of the waveguide (i.e. the light propagation axis from left to right), this appears to be a extremely similar system to the multilayer film that was considered earlier. Here, the regions along the axis of the where there is no hole corresponds to a layer of high refractive index, while the regions with an air hole in the waveguide corresponds to a layer with lower index. By modifying the dimensions of the hole, we can then modify the index contrast of the layers as well as their relative thicknesses, which would then affect the band structure, allowing us to engineer a band gap for a desired frequency.

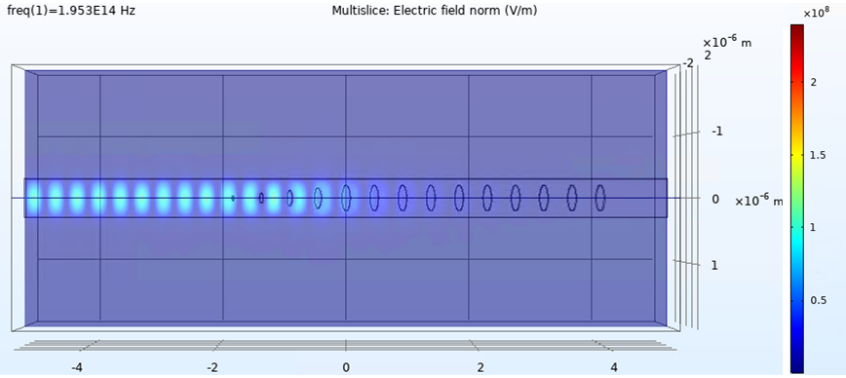

Figure 2.4: Schematic of waveguide with elliptical periodic holes in it acting as a photonic crystal. The light propagates from left to right along the silicon rectangular waveguide.

Firstly, we note that that the regions along the waveguide with a hole can be intuitively understood to have an effective dielectric constant that is an "average" of the area occupied by air and the area occupied by the silicon. Thus, if the holes were to be stretched vertically (perpendicular to the wavelength propagation direction), then the area occupied by the air hole would increase and thus decrease the dielectric constant for that layer. On the other hand, if we were to stretch the holes horizontally (parallel to the propagation direction), this would increase the thickness of the lower-index layer relative to the higher-index layer and thus also shift the frequency bands.

In this case, however, it is not possible to solve it analytically and we will need to numerically solve for the dispersion relation $\omega(k)$ to determine if there is a band gap at the desired light frequency.

2.3 Acid fiber etching

There are two common methods of creating tapered optical fibers, namely through the pulling of heated optical fibers [41] and the chemical etching of the fibers [36]. The pulling method involves using a heat source such as a laser [41] or flame [42] to heat the optical fiber while it is clamped on both sides and pulled at a specified rate by a translation stage, with the heating rate and pulling rate both playing a role in determining the final geometry of the taper.

In contrast, the simplest form of the acid etching method, known as meniscus etching, only requires the presence of HF with an inert chemical layer above the etchant. Other variations exist where dilutions of HF, such as buffered HF (a mixture of HF and NH_4F), are used instead for a slower and more controllable etch rate [43].

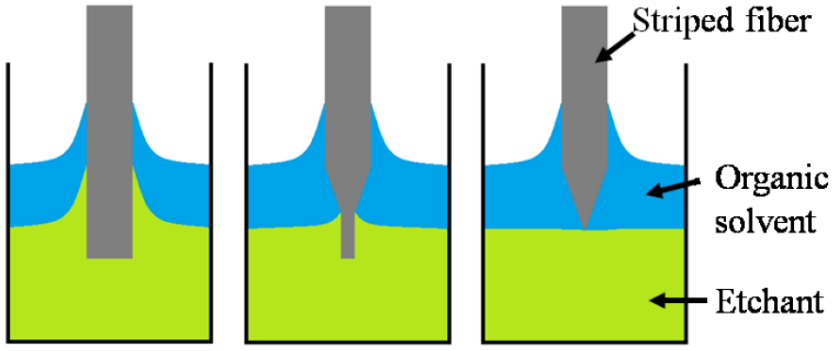

Figure 2.5: Schematic illustrating the mechanism of meniscus etching using an etchant (hydrofluoric acid) and an organic solvent layer. Image from [43].

In this process (schematic shown in Fig. 2.5), when the fiber is placed into the solution, surface tension causes the meniscus of both the etchant and the solvent is at a level higher than the overall water level. As time proceeds, the HF dissolves the fiber and causes its radius to decrease over time. This decreases the surface tension forces and causes the meniscus level to correspondingly fall in height over time. Therefore, the acid can only reach a smaller and smaller length along the fiber, causing the upper portions to remain thick while the bottom portions continue to get etched. This process continues until the lowermost portion of the fiber is completely dissolved, giving rise to a conical tapered fiber since the process occurs in a cylindrically symmetric manner.

In this process, the presence of the upper layer of organic solvent that is immiscible with water serves a twofold purpose. Firstly, it aids in washing off any remnant HF on the fiber and leads to cleaner tapers [36]. Secondly, it prevents HF from evaporating and causing surface roughness due to etching from the HF vapor. It has been demonstrated that the choice of organic solvent can lead to varying taper angles from 8° in nitrotoluene to 41° in 1-octanethiol [44], with a complicated dependence on the original fiber diameter, surface tension, and possibly other parameters.

Additionally, for a given choice of organic solvent, this method still has the potential for a wide variety of possible fiber taper geometries by translating the fiber up or down during the etching process. Depending on the translation direction and velocity, the taper lengths and angles can be modified in non-linear ways [45]. Fibers with more than one taper and tapers with differing taper angles can also be created, as shown in Fig. 2.6.

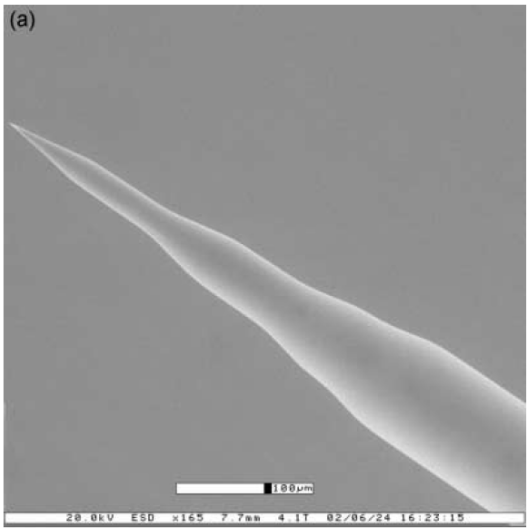

Figure 2.6: Sample fiber illustrating the possibility of creating fibers with multiple "steps" by translating the fiber at different velocities during the etching process in order to create more intricate fiber taper geometries. Image from [45].

Chapter 3

TAPER GEOMETRY DESIGN

In this chapter, we present the simulation results and final design for the tapered fiber, tapered waveguide, and photonic crystal mirrors. For the first two systems, we are mainly interested in varying the taper rates and relative alignment of the two tapers to achieve a gradual transition of the effective mode index and maximize transmission. The mode indices are computed for a frequency of $f = 195\,\text{THz}$, corresponding to a free-space wavelength of 1536 nm, which matches the transition energy of erbium that will be most useful for long-distance telecommunications as they have low optical fiber losses.

On the other hand, our aim for the photonic crystal mirror is to vary the crystal periodicity and the hole dimensions to achieve a band gap at the transition wavelength of $\lambda = 1536\,\text{nm}$ and maximize reflectivity.

All simulations were done using COMSOL Multiphysics Version 5.4 [46] Wave Optics module, which is a finite element solver that can solve for normal modes as well as the full 3D electric and magnetic field distribution given the boundary conditions.

In order to get a more concrete idea of how the entire fiber-waveguide coupling interface together with the photonic crystal mirror will look like, we present a schematic for the overall setup in Fig. 3.1. The fiber comes in from the top left and gradually tapers from an initial size to a minimum radius with some fixed taper angle. The waveguide lies below the fiber and "inverse tapers", i.e. it starts from a minimum width and gradually gets larger over some taper length until it reaches its maximum width. There is then a photonic crystal in the waveguide which will serve to reflect the light that has coupled from the fiber into the waveguide back into fiber, allowing us to detect the signal in a photodetector.

3.1 2D Tapered fiber & waveguide simulations

Before we embark on a full 3D simulation of the taper geometry, it is instructive to consider 2D simulations of their cross sections. Due to the relative computational simplicity of the 2D case, we are able to sweep over a larger area of parameter space to get an intuition for the behavior of the system as a function of various geometrical

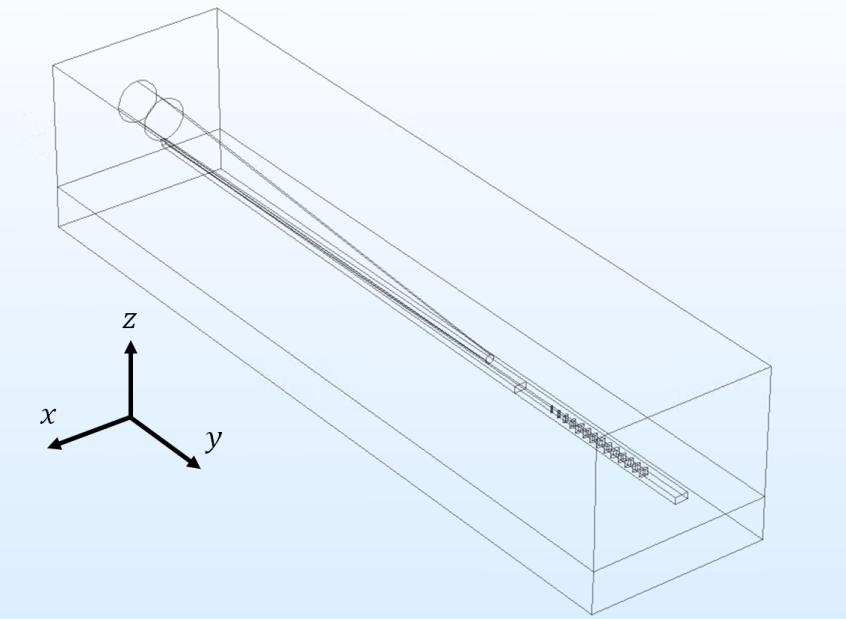

Figure 3.1: Geometry of tapered fiber coupling to a tapered waveguide with a photonic crystal mirror.

parameters. At the same time, obtaining the relations between the effective mode indices allows us estimate the maximum taper rate as determined by the adiabatic condition.

2D fiber cross-sections

We start with 2D simulations of cross-sections of the fiber at various fiber radii. The maximum radius that we consider is 4 µm since that is the core radius of the SMF-28e+ fiber that we will be using [13].

Fig. 3.2 shows the effective mode indices for the fundamental mode and the first excited fiber mode, where the mode shapes are shown in Fig. 3.3. It can be seen that the fiber no longer supports excited modes once its radius is shrunk below approximately 550 nm, and no longer supports the fundamental mode below 250 nm radius.

Therefore, this indicates that we should aim to taper the fiber to a minimum radius of approximately 250 nm or less, so that most of the optical power traveling within the fiber will eventually leak out the fiber and couple into the waveguide as desired. At the same time, by applying the adiabatic condition from equation 2.16 and using the value of n_{eff} at $r = 4\,\mu\text{m}$ since the index difference is smallest there, we obtain the result that the taper half-angle should be smaller than 1.5° in order to satisfy the

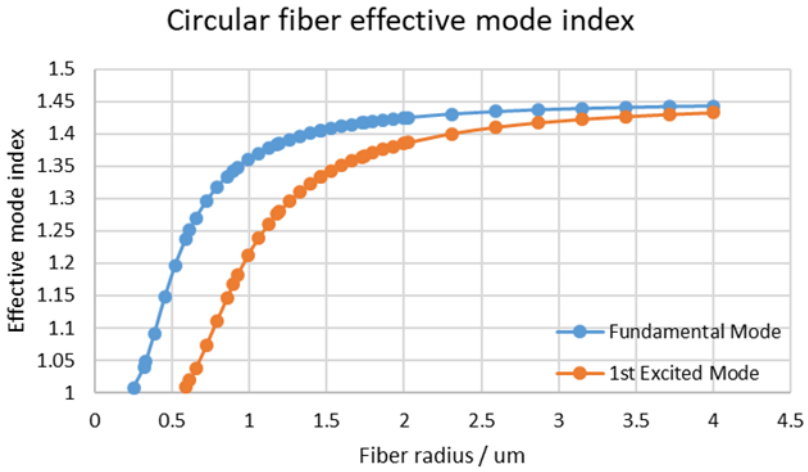

Figure 3.2: Effective mode indices of the fiber against fiber radius

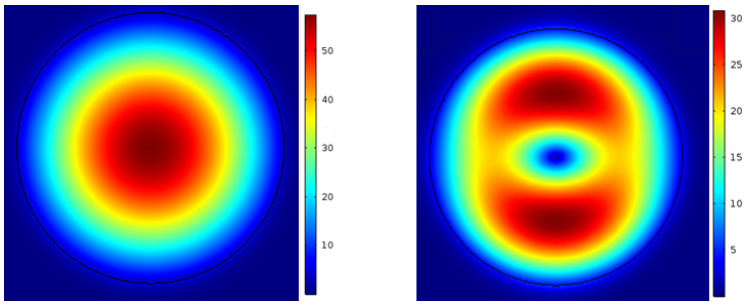

Figure 3.3: Fiber fundamental mode and first excited mode. Colors represent electric field magnitude in Vm^{-1}.

adiabatic condition for minimal power loss.

2D waveguide cross-sections

We now turn our attention to the simulation of 2D cross-sections of the rectangular waveguide with varying waveguide widths. The waveguide height is fixed to be a constant 300 nm due to limitations of the fabrication process as will be discussed in section 4.2. In this case, unlike the fiber which had two planes of symmetry, we need to distinguish between the TM and TE polarization modes which have different mode indices. In particular, we are interested in the TM modes because as shown in Fig. 3.4, the fundamental TM mode has a larger the maximum fraction of the electric field located above and below the waveguide. Since we are interested in using the evanescent fields from the waveguide to couple to rare-earth ions in the crystal located below the waveguide, it is desirable to have the light in the fundamental TM mode.

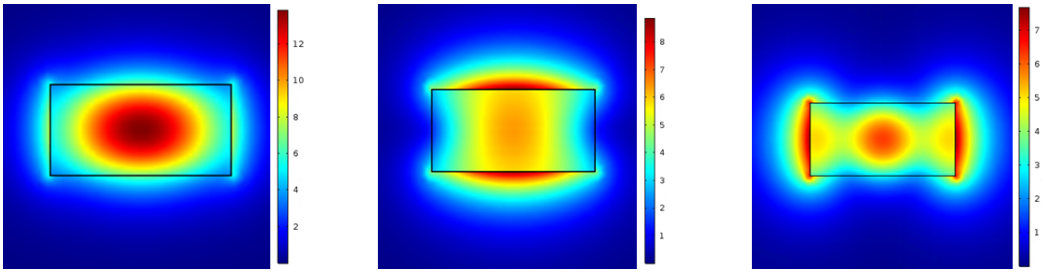

Figure 3.4: From left to right: Waveguide fundamental TE mode, fundamental TM mode, and first excited TM mode. Colors represent electric field magnitude in Vm^{-1}.

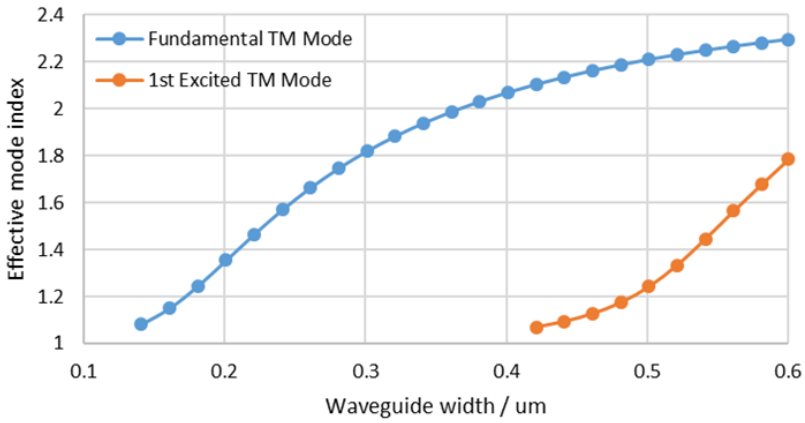

Figure 3.5: Effective mode indices of Si waveguide against waveguide width

The effective mode indices for the fundamental TM mode and the first excited TM mode are shown in Fig. 3.5. In this case, the waveguide no longer supports excited TM modes once its width goes below approximately 420 nm, and no longer supports the fundamental mode when its width is below 140 nm. This again indicates that we should aim to taper the waveguide down to a width of approximately 100 nm so that power from the fiber can efficiently couple into the waveguide.

We can again apply the adiabatic condition to onto the values of the effective mode indices for the fundamental and excited TM modes to find that the maximum taper half-angle is approximately 11°. We can neglect the TE modes since they are of an opposite parity with respect to mirror symmetry and thus we will not get coupling between TM and TE modes assuming the overall setup is symmetric about left-right reflection.

2D fiber-waveguide coupling

Having understood how the fundamental mode indices for the fiber and waveguide vary as they are tapered, we now want to consider how the effective mode index changes in the combined systems of the fiber and silicon waveguide. In order to do this, we simulate a series of 2D-cross sections where a fiber is placed on top of a rectangular silicon waveguide. The fiber radius is then decreased while the waveguide width is increased at the same time in order to simulate the various cross-sections of the system along the axial-position. The basic setup is shown in Fig. 3.6 where the slices indicates the series of 2D cross-section simulations that we will be doing, and the direction of the y axis is indicated.

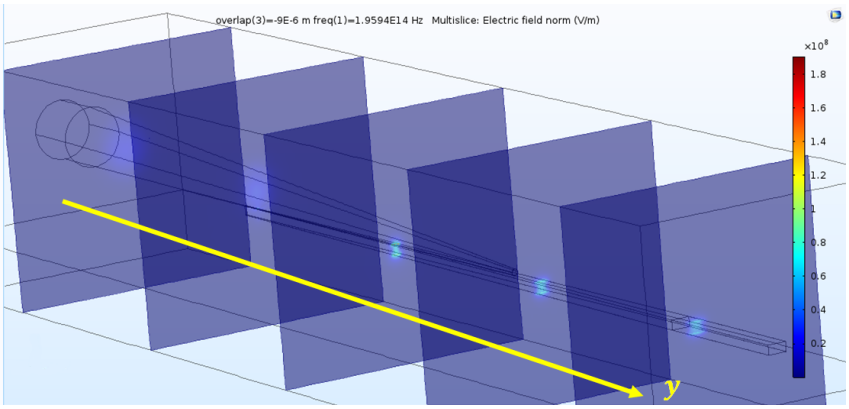

Figure 3.6: Schematic of 2D cross-section slices of the taper interface that we simulate. The fiber gets thinner while the waveguide gets wider in the direction of increasing y.

For each cross-section, we solve the eigenvalue equation to obtain the mode shape and effective mode index of the fundamental mode in this fiber-waveguide combined geometry, which we call the hybrid mode or supermode since the light spans across both the fiber and the waveguide. We can then obtain a rough estimate for whether the coupling will have high or low transmittance by observing the supermode effective mode index, where we expect that a gradual and smooth transition of the supermode index along the axis should lead to a high transmittance. This is because rapid changes to the mode index across a short distance would lead to reflection (which can be intuitively understood by considering the extreme case where there is a step change in wave speed across a material interface), while slow changes would obey the adiabatic condition for minimal losses.

In order to achieve this, there are several degrees of freedom that we can manipulate, namely the taper rates, the relative positions of the fiber and waveguide, as well as

the final tip radius/width of the fiber/waveguide. The maximum possible radius of the fiber is upper bounded by 4 µm since that is the initial core radius before etching, while the maximum width of the waveguide is fixed to be 600 nm.

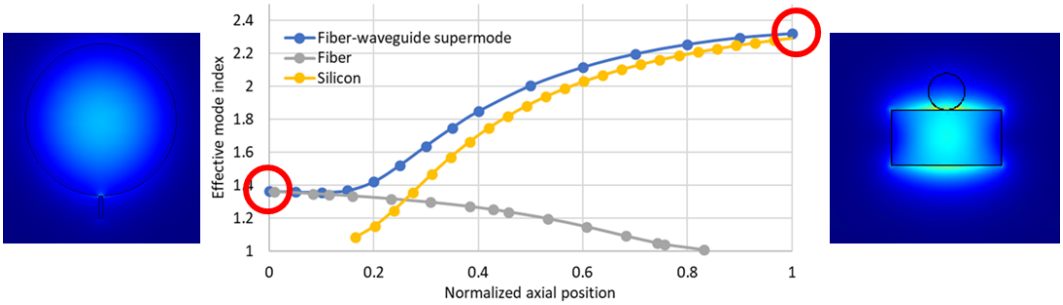

Figure 3.7: Effective mode indices of fiber-waveguide supermode. The fiber's radius is tapered from 1 µm to 100 nm while the waveguide's width is increased from 50 nm to 600 nm along the axial coordinate. The images show the mode's electric field distribution at the two ends of the taper region.

Fig. 3.7 shows the resulting supermode index after optimization of the above parameters. We can fully specify a particular geometry by specifying the fiber radius and waveguide width at the two endpoints of the fiber-waveguide overlap region (Fig. 3.1 shows a schematic of the relevant parameters). In this plot, the fiber's minimum radius was set to be 100 nm, and the waveguide is set to be 600 nm wide at this point; at the other endpoint, the minimum waveguide width was 50 nm and the fiber radius was 1 µm at this point.

The x-axis in Fig. 3.7 is a normalized position y along the fiber axis direction. Since our simulation is purely 2D, the absolute taper rates do not matter (only the relative taper rates) and thus we can normalize the coordinates such that $y = 0$ refers to the point where the waveguide is narrowest and $y = 1$ is where the fiber is thinnest. The effective mode indices of the fundamental modes for the fiber and waveguides on their own have also been overlaid onto the plot, where these indices are identical to those shown in Figs 3.2 and 3.5 (aside from reflection and translation) and do not account for any shifts in index due to the mutual interaction.

At the same time, the magnitude of the electric field for the fiber-waveguide hybridized supermode is shown for the two endpoints of this taper region region. The mode distribution is exactly as we expected, with most of the optical power located in the fiber at $y = 0$ since the waveguide is much too narrow to support even the fundamental mode. Looking at the supermode index, we also see that at this point the

supermode index is almost identical to the mode index when we only had the fiber present (gray line). This makes sense since the electric field is mostly concentrated in the fiber and thus should not be affected by the presence of the waveguide.

As we move along the axial direction, the electric field gradually shifts towards the waveguide. We do indeed see a smooth and gradual evolution of the supermode index as it tends towards the mode index computed with only the waveguide present (yellow line), and thus we expect a transmission coefficient of near unity once we simulate this geometry in a 3D simulation. The image of the field distribution also shows most of the power located in the waveguide, since it is the fiber that is now too thin to support wave propagation.

3.2 3D Tapered fiber & waveguide simulations

With the 2D simulations in the previous section providing us with a set of geometrical parameters for the fiber and waveguide that we might expect to have high transmission, it is now necessary to perform a full 3D simulation in order to obtain the resulting spatial field distribution and transmittance.

From the previous section, we found that the choice of fiber taper radius from 1 μm to 100 nm as well as waveguide taper width from 50 nm to 600 nm appeared to be a promising taper geometry for us to achieve a high transmittance and thus coupling efficiency between the fiber and the waveguide, and thus we will stick with this choice of parameters.

However, now that we are doing a 3D simulation, we have an additional degree of freedom for the geometry, namely the taper rates along the axis. In other words, we need to decide the axial length of the taper. While this would not affect the 2D simulations earlier (since we were simply taking cross-section slices), this would have a huge impact on the actual 3D field distribution since too fast a taper rate would lead to a rapid change in the mode index along the propagation axis, leading to a violation of the adiabatic condition as we discussed in Section 2.1 and cause coupling to higher order modes as well as scattering or reflection.

We decided to start with a choice of waveguide taper length of 25 μm, as this was the longest taper length that we had confidence, based on past experience, in fabricating without a high likelihood of the taper breaking during the process. On the other hand, we chose a fiber taper half-angle of 2° for our initial simulations, which gave rise to a taper length of 25.8 μm, which is almost equal to the waveguide taper length. While this is slightly larger than the adiabatic condition bound of 1.5° that we found

in section 2.1, we chose this value of fiber taper angle in order to correspond more closely with the taper angles of our initial fiber fabrication attempts. As we will see in the next section, this taper angle is still gradual enough to transfer almost all of the incoming optical power into the waveguide.

Fiber-waveguide transmission measurements

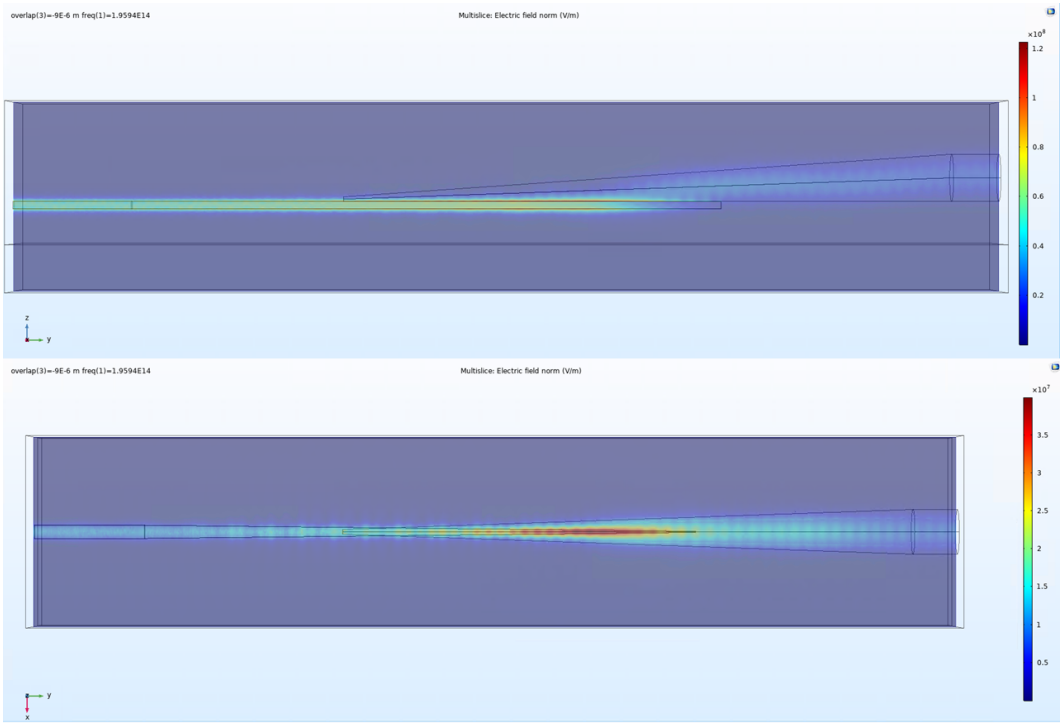

Figure 3.8: 3D simulation of the geometry design that was discussed in section 3.1 with taper half-angle 2° and the waveguide tapering over a length of 25 µm. The simulation shows views from two angles, with the colormap representing the electric field intensity.

Figure 3.8 shows a sample 3D simulation that was conducted, where the colormap represents the electric field intensity. Light is sent into the fiber end (right side of the plot) in the fundamental mode and the transmitted light at the output port at the waveguide end (left boundary) is computed. From this, we are able to obtain from the simulation a measure of the transmittance, reflectance and absorbance of the light propagation, where absorbance also includes light that is scattered at the interface and goes off to infinity since we place scattering boundary conditions on the bounding box of the simulation. All of the 3D simulation results below rely on simulations of this type that allows us to extract the transmission coefficient.

The two plots above show two different angles of the coupling interface, where

the top plot shows the side view, allowing us to see the fiber lying on top of the waveguide. From this side view, we can see that the incoming power from the fiber does indeed couple down into the waveguide and then travel out towards the output port on the left. The bottom plot shows a top view of the system, allowing us to see the taper of the fiber as well as the taper of the waveguide. In particular, we see that there is a maximum intensity of the electric field near the region where the waveguide is at its narrowest. Additionally, for this simulation and all others in this section, we add in the geometry a fiber region of constant radius (length 2 μm) and a waveguide region of constant width (length 5 μm), as can be seen in the right and left sides of the plots respectively. This is to ensure that the propagating light at the input and output ports reach steady state before/after they encounter the interaction region between the fiber and waveguide so as to obtain an accurate computed result.

Axial position dependence

Our first test of the performance of this set of taper parameters is to set up the geometry and compute the transmittance from the fiber to the waveguide as we place the fiber at different axial positions along the central axis, which is the y-axis in Fig. 3.1. The reason for doing this sweep along the fiber axial position is twofold. Firstly, this is to compensate for the fact that we have chosen a fiber taper length (based on our choice of taper half-angle of 2°) of 25.8 μm that was slightly longer than the waveguide's taper length of 25 μm. As such, the point at which the waveguide reaches its minimum width would no longer coincide with the fiber's point of maximum radius, which represents a small deviation from the geometry computed in the 2D case that would need to compensated for. More importantly, this tells us how much resolution in the fiber position we will require in the experimental stage in order for us to achieve a good coupling. If the transmittance only peaks at a very particular fiber position, this would mean that it is difficult to do the alignment experimentally since we would need to place the fiber within that very small target region.

The results are shown in Fig. 3.9, and fortunately we see that there is a wide window of axial positions of at least 10 μm where there is a high transmittance of over 95%. This means that we can afford to have some error in the positioning of the fiber and still expect to see good coupling efficiencies. The peak transmittance was found to be 99.5% at axial position offset −9 μm, where 0 axial offset refers to the position where the fiber's tapered tip is directly above the waveguide's point of maximum

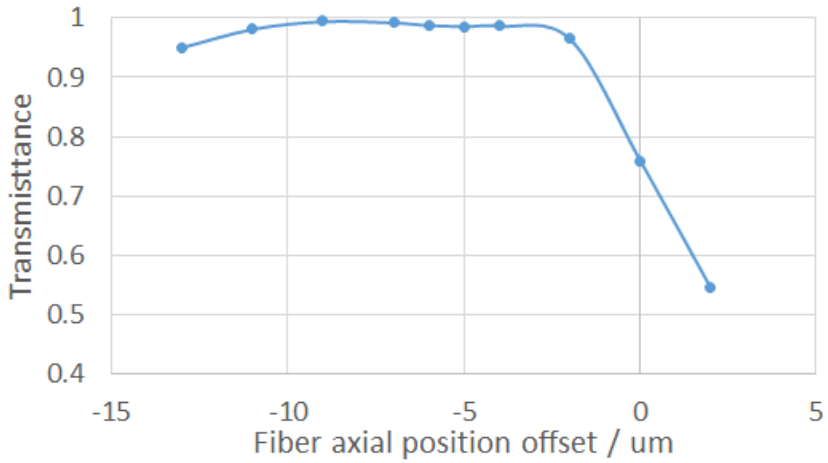

Figure 3.9: Transmittance against fiber transverse position with a maximum of 99.5% at −9 µm offset. The 0 axial offset position refers to the position where the fiber's tapered tip is directly above the waveguide's point of maximum width. The sign of the axial position is defined in the same way as the y-axis in Fig 3.1.

width.

Transverse position dependence

We can also do the same sweep of the fiber position but this time in the transverse direction, which is the x-axis in Fig. 3.1. Here, the natural point of reference for 0 offset position is chosen to be the central symmetry plane of the tapered fiber/waveguide system.

The results are shown in Fig. 3.10 where the axial position offset is fixed at −9 µm which gave the maximum transmittance from the previous sweep. As we might expect, we observe the largest transmittance of 99.5% when the offset is 0, i.e. when the fiber is placed along the central symmetry plane. This makes sense since there is a maximum overlap area between the fiber and the waveguide when they are both aligned along the symmetry plane. By displacing the fiber off-axis, the light that is "leaked" out of the fiber when the fiber becomes too small to support the mode would be coupled out into the air instead of into the waveguide as desired, which lowers the transmitted power.

One point of note is that the x-axis tolerance in this case is much smaller compared to the axial position. In particular, we see that we need the offset to be less than approximately 0.1 µm in order to achieve a transmittance of 95% or higher. This might be due to the fact that when we shift the fiber off-axis, the part of the

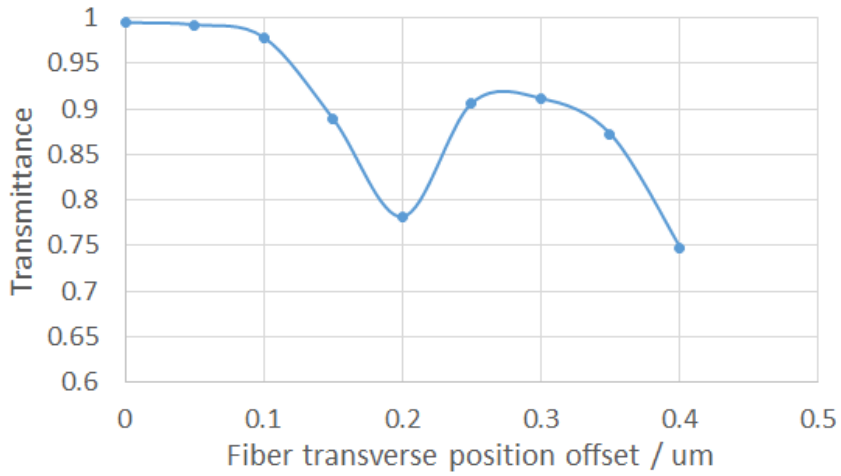

Figure 3.10: Transmittance against fiber transverse position when axial position offset is fixed at −9 µm. The maximum is at zero offset with transmittance 99.5%. Note the much smaller x-axis scale compared to Fig. 3.9, meaning that it is much more sensitive to deviations from being perfectly centered.

fiber that is above the narrowest portion of the waveguide (50 nm) is quickly no longer in contact with the waveguide, leading to large amounts of losses in those regions. Therefore, the implication is that we require much tighter tolerances in the transverse positioning of the fiber on the waveguide if we wish to have a good coupling efficiency.

Taper rate dependence

Having verified that our choice of minimum/maximum radii and widths as well as taper rate does indeed give rise to a reasonably high maximum transmittance of 99.5% given the right fiber positioning, we will now also investigate the effect of different fiber taper rates. This will let us know the amount of tolerance we need to have on the taper angle of the fibers that we need to manufacture.

We show the results of the simulation for taper half-angles of $1°, 2°, 4°$ and $8°$ in Fig. 3.11. For these 4 taper angles, we observe a maximum simulated transmittance of 98.7%, 99.5%, 98.8%, and 78.5% respectively. This therefore tells us that even if our fiber fabrication process had relatively low control over the taper angle, we should still be able to achieve high transmittances over 98% as long as our taper half-angle is $4°$ or less. This gives us some leeway in terms of our experimental tolerance for the fiber fabrication.

One point of note is that the $1°$ taper appears to perform worse than the $2°$ and $4°$

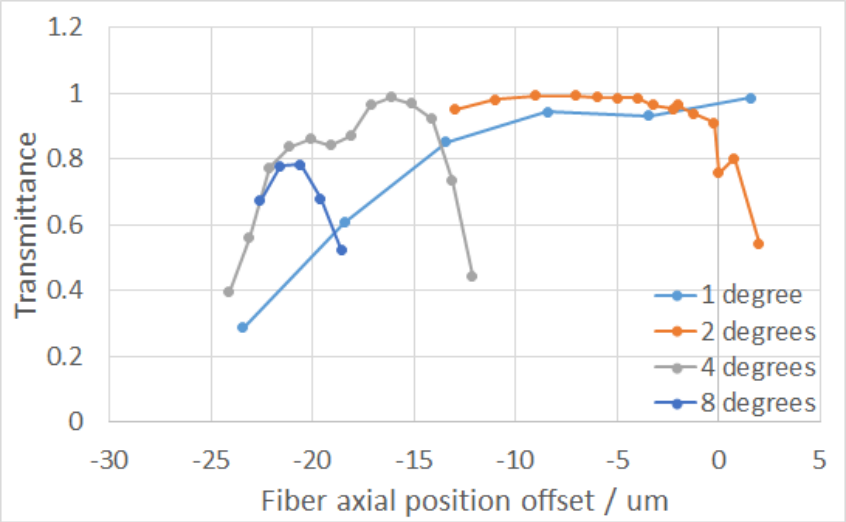

Figure 3.11: Transmittance against fiber axial position for various fiber taper angles.

fiber, which seems contradictory to our expectations that it should perform better due to its more gradual taper. We believe this might be because we have not fully optimized for the optimum axial position for that fiber, seeing that the graph appears to possibly continue increasing towards the right. However, this current search range for the axial position is sufficient for our current purpose in this section of providing a lower bound on the performance of fibers with various taper angles.

Another interesting trend is the fact that the optimum axial position offset appears to be shifting left as we increase the taper angle. This leftward shift in the plot indicates that we are pulling the fiber in the $-y$ direction, i.e. further away from the waveguide. We believe is this because when we compare a fiber with a larger taper angle compared to one with a smaller angle, the one with the larger angle will have a smaller radius at each given point along the axis since it tapers off faster. Therefore, if we were to keep the same axial position, the ratio of the fiber radius compared to the waveguide width at each point would be smaller than optimum, and we would therefore want to move the fiber in the $-y$ direction in order to maintain the same ratio of the fiber radius to waveguide width as before.

Simulation convergence

Finally, because our simulation results will depend on the meshing of the system into finite domains so that finite-element analysis can be done by COMSOL, it is imperative to verify that the meshing that we choose is sufficiently fine that we avoid any numerical errors from this discretization of space. To test our meshing settings,

we simulate the transmittance for two different values of fiber axial positions and each with a varying level of mesh fineness. The mesh fineness was adjusted by scaling each length scale in the COMSOL meshing settings by a constant factor.

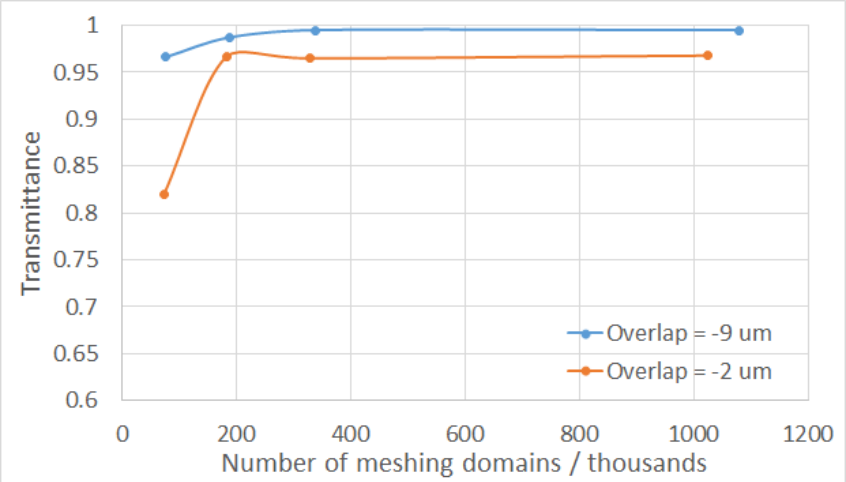

Figure 3.12: Transmittance against number of meshing domain elements for two different axial positions for the fiber.

The results are shown in Fig. 3.12, where the mesh settings for the simulations shown in previous sections corresponds to the point located at approximately 340,000 domain elements. We see that the computed transmittance is almost identical to the result computed using over 1 million domain elements. Comparing the actual numerical results reveals a difference of less than 0.3%. While we also attempted to use a larger number of domains for testing, our computing cluster was unable to run the simulation entirely within its RAM, leading to drastically slowed-down computation times. On the other hand, when we reduced the number of domains, we see that the performance begins to deviate from the more accurate results obtained using more elements. Therefore, we are confident that our choice of mesh fineness is accurate and represents a good tradeoff between computation time and accuracy.

3.3 Photonic crystal simulations

For the design of the photonic crystal, our goal is to come up with holes in the silicon waveguide of a certain dimension and period such that we obtain a band gap at the light propagation frequency of 195 THz, as this would prevent the propagation through the photonic crystal, causing the light to reflect and thus acting like a high-efficiency mirror.

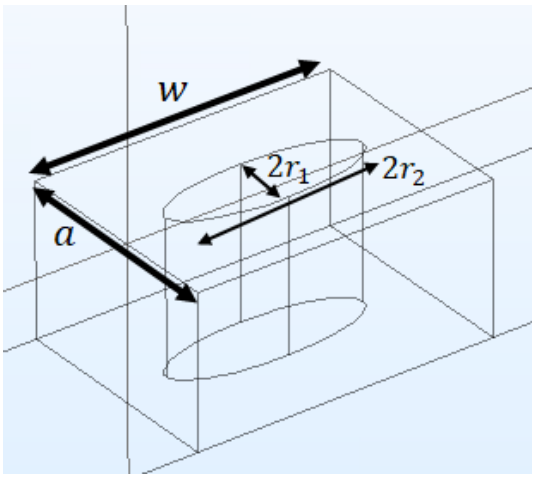

Figure 3.13: Photonic crystal unit cell

Periodic cell photonic crystal

Since a photonic crystal on a waveguide is by definition a periodic structure, we can simplify the simulation geometry and reduce computation time by creating a unit cell and then applying periodic boundary conditions. Fig. 3.13 shows the relevant parameters of the crystal, where $w = 600\,\text{nm}$ is fixed at the waveguide's maximum width while the period a and hole dimensions r_1 and r_2 are optimized. We sweep across values for these parameters and compute the set of possible optical mode frequencies supported by that periodic structure for each possible wavenumber k.

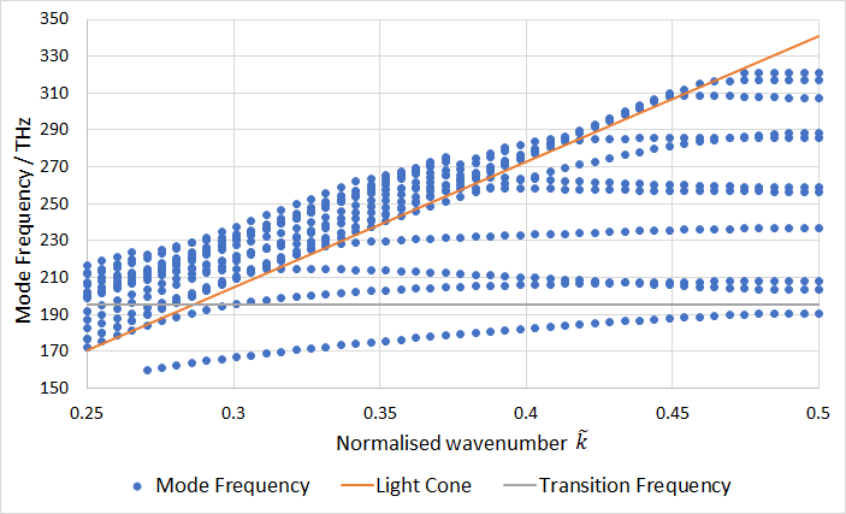

Figure 3.14: Photonic crystal band structure with $a = 440\,\text{nm}$, $r_1 = 65\,\text{nm}$, $r_2 = 200\,\text{nm}$ with a partial band gap at light propagation frequency of 195 THz.

Fig. 3.14 shows the band structure of the optimized photonic crystal with dimensions

$a = 440\,\text{nm}, r_1 = 65\,\text{nm}, r_2 = 200\,\text{nm}$. The x-axis plots the normalized wavenumber $\tilde{k} = \frac{ka}{2\pi}$ and the y-axis is the mode frequency in THz. The orange line is the light line where we have continuous free modes above the line and discrete index-guided bound modes below the line [37], while the horizontal gray line plots the frequency of 195 THz corresponding to the frequency of light that want to create a band gap for.

As we can see, the gray line does not intersect any particular mode for values of $\tilde{k} > 0.3$. While we do not have a complete photonic band gap, the large range of wavenumbers with no supported modes indicates that we should expect this design to perform reasonably well as a mirror.

Finite-length photonic crystals

To further test this choice of hole dimensions, we therefore performed a full 3D simulation in COMSOL where we placed holes of the above size into a silicon waveguide of height 300 nm and constant width 600 nm. Light at 195 THz was then made to propagate down the waveguide, following which the transmittance and reflectance could be computed.

To begin, we first needed an estimate of how many holes were needed to achieve a reasonable reflectance, since the simulation in the previous section assumed an infinite periodic structure which is impossible to realize. In our initial trials, we placed into the waveguide 10 identical holes with dimensions from the previous section and obtained a reflectance of 0.835, a transmittance if 0.014, and an absorptance (including scattering) of 0.152. The relatively high fraction of light scattered thus suggests that there is a mode mismatch caused by a sudden change in the propagation modes at the onset of the holes. We also performed an additional preliminary test where we placed 18 holes with the same size and found a reflectance of 0.842 and an absorptance of 0.157. These results support the intuition that there is a sharp index boundary at the onset of the holes that causes the high scattering instead of us just having an insufficient number of holes, since the reflectance was almost unchanged despite almost doubling the number of holes.

In order to verify this hypothesis, 4 additional holes with dimensions that were $0.2, 0.4, 0.6$ and 0.8 times the dimensions of the mirror holes were placed before the row of 10 holes. This allows the mode index to transition smoothly from the bulk silicon into the mirror region, and we indeed observe an improved reflectance of 0.984 and a reduced absorptance of 0.0113. We will therefore use this choice of 4

holes with linearly-tapered size in all designs from now on.

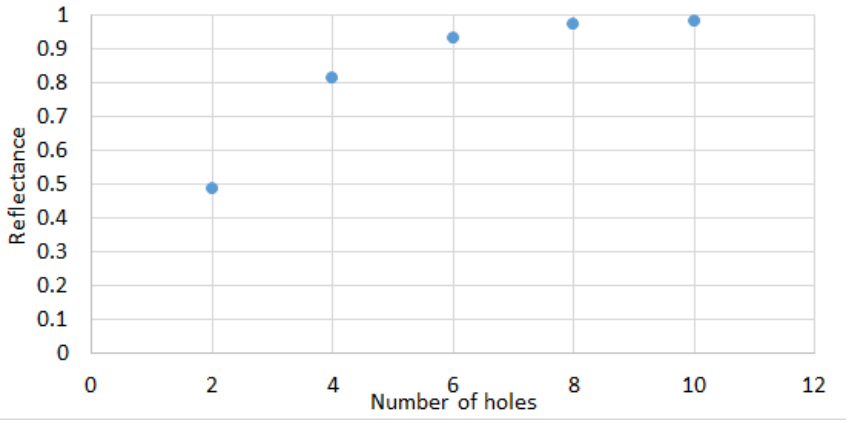

Figure 3.15: Reflectance dependence on number of photonic crystal holes

Following this, we decided to determine the number of holes necessary in the mirror region to achieve a reasonable reflectance, and the results are shown in Fig. 3.15. We see that our initial choice of 10 holes appears to be already in the saturation region for the reflectance. Subsequent tests using more holes did not yield a significant increase in the reflectance.

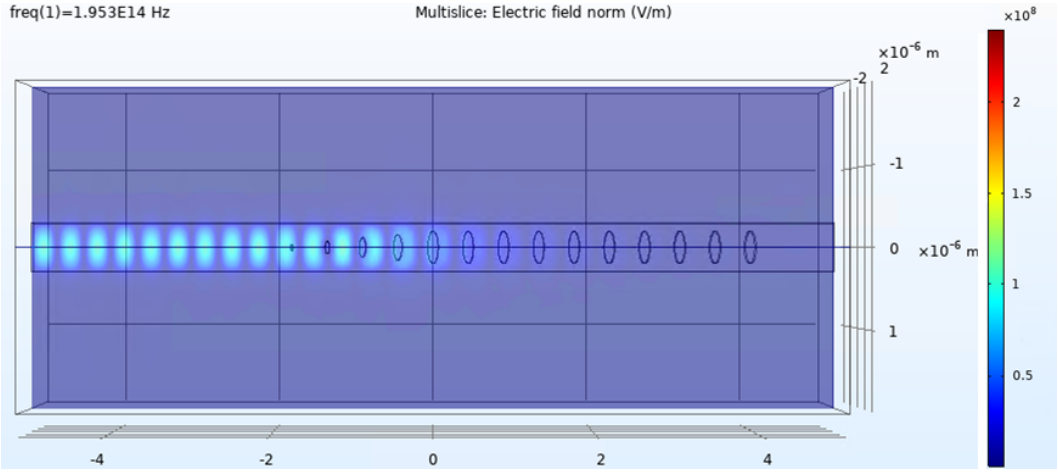

Figure 3.16: Light propagation through the photonic crystal mirror with 10 mirror holes and 4 tapered holes. The color plots the norm of the electric field.

We can also verify that most of the light is being reflected by simulating and plotting the electric field distribution, which is shown in Fig. 3.16. As we expected, the incoming light from the left does not make it past the first few holes before being reflected, and there is almost zero field past the fifth hole in the constant-radius

region. We also observe little electric field outside of the waveguide, indicating that there is also little loss to scattering as the previous calculations indicated.

Another important parameter of the photonic crystal mirror is the bandwidth, which measures the range of wavelengths for the incoming light that it can effectively reflect. This is important since the incoming light might not all have the exact target wavelength of 1536 nm.

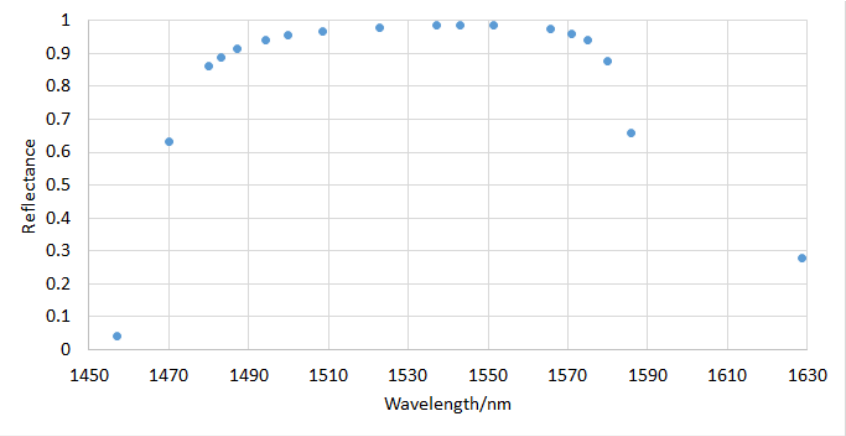

Figure 3.17: Reflectance against incoming light wavelength

From Fig. 3.17, we find that our photonic crystal mirror has a bandwidth of approximately 93 nm centered around 1531 nm where we have a reflectance of 90% or higher. This wide bandwidth is therefore sufficient for our purposes since we do not expect our laser or emission sources to be anywhere near this broad.

Silicon support beams

Having fixed the geometry of the photonic crystal holes to maximize reflection from the end of the waveguide, another degree of freedom in the design of the waveguide was whether or not to include support beams that would connect the waveguide to the side walls of the top silicon layer to provide additional structural support and prevent breakage of the waveguide taper due to stresses during the fabrication process. In addition, the width and position of these support beams would need to be optimized in order to minimize any leakage of optical power through them as well as minimize any interference with the reflectivity of the photonic crystal cavity. We first tackle the problem of power leakage through the beams.

To estimate the impact of the silicon beams on the transmission of power through the waveguide, we simulated a waveguide that was 10 µm long, 600 nm wide, and

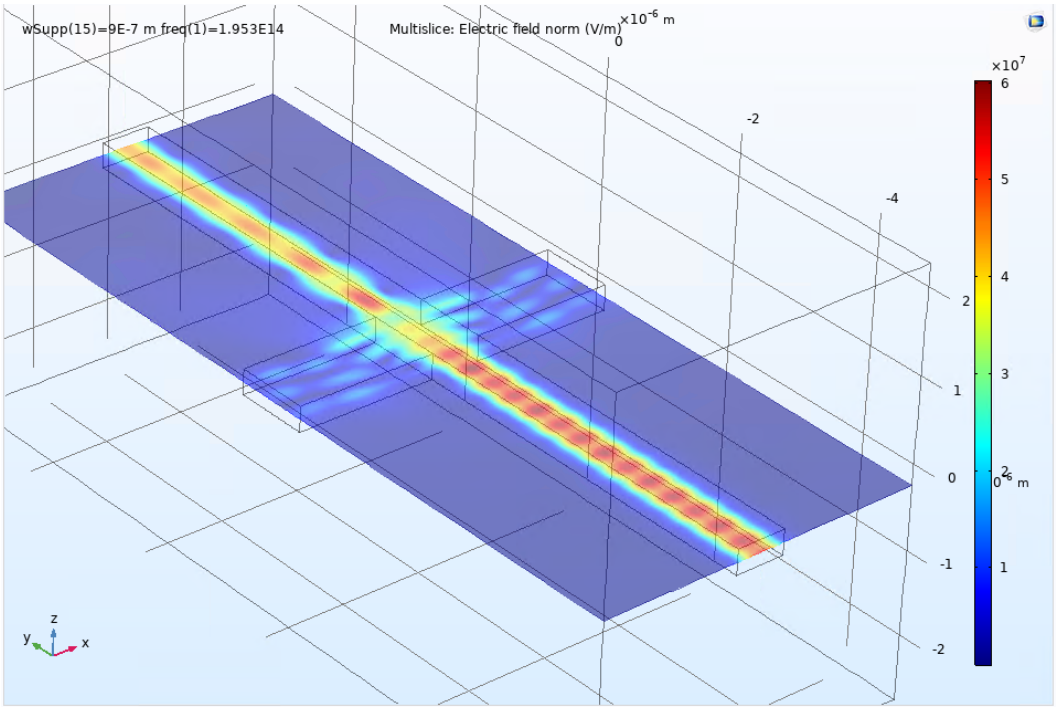

Figure 3.18: Illustration of optical power leaking through the support beams with width 900 nm, where the colormap represents electric field magnitude.

300 nm thick. One silicon support beam of length 1.7 µm was then placed on either side of the waveguide at the midpoint of the length, and scattering boundary conditions was applied to the external boundary of the beams. Light was then sent into the waveguide in the fundamental TM mode and the power transmitted to the other end of the waveguide was computed. As can be seen in Fig. 3.18, when the support beam is too wide as in this case where its width was 900 nm, there is significant coupling of the incoming light out to the support beams where the energy is lost.

More systematically, we then varied the widths of the support beams and plotted the simulated transmittances as shown in Fig. 3.19. As expected, the transmittance falls as the support width increases since more light gets coupled into the wider beam out of the waveguide. In order to achieve a transmittance of more than 90%, we are therefore forced to only consider support beams with widths 300 nm or smaller.

At the same time, we also need to determine the positions of the support beams relative to the photonic crystal holes that will be patterned onto the waveguide. As can be seen from the preliminary testing in Fig. 3.20 where we placed the support beams 3 µm behind of the photonic crystal holes (left half of figure) compared to

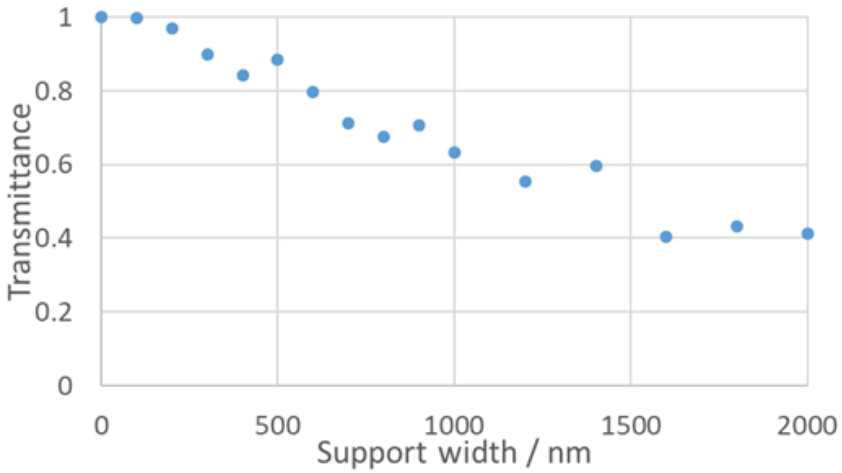

Figure 3.19: Transmittance against width of silicon support beams, showing a clear leakage of power through the beams as they get wider.

3 µm in front of the holes (right half of figure), there is a much greater proportion of power that is lost through the supports when placed in front of the holes. This can be explained simply by the fact that there is little field intensity in the region behind the photonic crystal holes in the first place since most of the power has already been reflected back, and thus placing support beams there should not affect the system's behavior. Indeed, we see that the left geometry has a reflectance of 97.0% compared to 68.9% for the right geometry, where both geometries used support beams of width 500 nm.

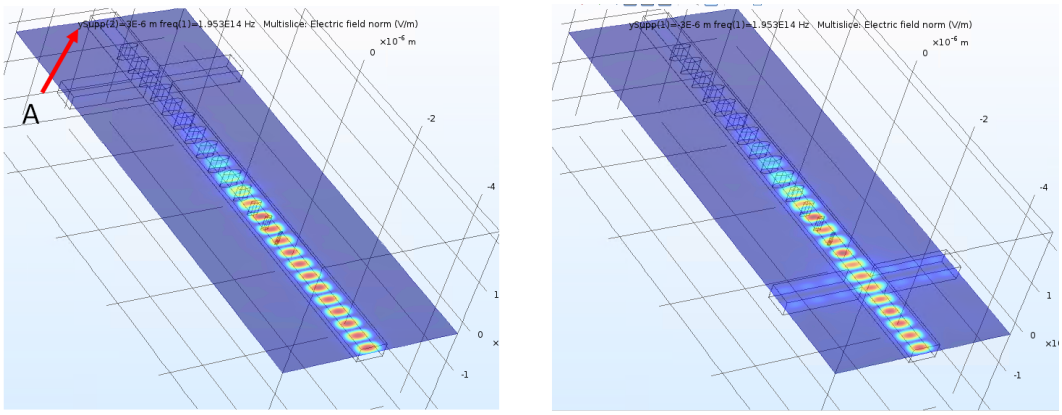

Figure 3.20: Electric field propagation for support beams at different positions.

While it is indeed true that placing support beams behind the photonic crystals would lead to the best reflectance performance, it would not make sense from a structural stability point of view, since the waveguide is anchored to the surrounding silicon

Fiber min radius	100 nm
Fiber max radius	1 μm
Fiber taper half-angle	$1^\circ \sim 4^\circ$
Axial positioning accuracy	$\sim$ 10 μm
Transverse positioning accuracy	$\sim$ 0.1 μm
Waveguide min width	50 nm
Waveguide max width	600 nm
Photonic crystal r_1	65 nm
Photonic crystal r_2	200 nm
Photonic crystal period a	440 nm
Number of photonic crystal holes	10 + 4 taper holes ($0.2, 0.4, 0.6, 0.8\times$ sized)
Support beam width	300 nm
Support beam position	5 μm before photonic crystal holes
Expected overall reflectance	0.842

Table 3.1: Summary of geometrical parameters for the fiber-waveguide coupling interface from the simulations.

layer at point *A* in Fig. 3.20, and thus the supports would not provide much stability for the waveguide as it is too close to the anchor point.

As such, for our final design, we chose to place silicon support beams width 300 nm placed 5 μm in front of the photonic crystal holes in order to balance the contribution to structural stability and the negative impact on reflectance. The reflectance of this photonic crystal with support beams was simulated to be 0.842.

3.4 Final taper geometry design

In summary, from the simulations in this chapter, we summarize our target geometry for the fiber and waveguide fabrication in table 3.1.

For this choice of geometrical parameters, we expect that for the optimal fiber positioning, we should be able to get 0.995 efficiency coupling from the fiber into the waveguide. Following that, it should experience a reflection at the photonic crystal mirror with reflectance 0.842, followed by coupling back into the fiber with 0.995 efficiency. The overall expected reflected intensity is thus the product of these quantities, giving an overall reflectance of 0.836.

Here, we have assumed that the fiber-waveguide coupling interface and the photonic crystal mirror are independent and do not affect the properties of each other. In reality, this assumption may not be fully accurate since they are located relatively nearby and thus the shape of the electric field distribution might be distorted by

the presence of the other structure. Therefore, in order to compute a more accurate estimate of the overall reflectance of this structure, it would be ideal to simulate the entire structure as shown in Fig. 3.1 as a single geometry in order to account for all the coupling between components of the system. However, we were unable to do this in this project as there are structures with many different length scales in this geometry, making the meshing and numerical convergence difficult as well as time-consuming. Nevertheless, we expect that there should the effect of this interference should be minimal as the tip of the fiber is placed several microns away from the support beams, which corresponds to several wavelengths of distance since $\lambda_0 = 1536\,\text{nm}$.

Chapter 4

EXPERIMENTAL METHODS & SETUP

This chapter describes in detail the procedures for the three main portions of the experimental setup – etching the fiber to form a taper, etching the silicon wafer to make a tapered waveguide and a photonic crystal mirror, and aligning the fiber with the waveguide to measure the coupling efficiency of the interface.

4.1 Optical fiber etching

Setup construction

The overall setup used for the etching of the optical fiber is shown in Fig. 4.1 with the important components labelled. The key components of the etching setup are: (1) fiber holder used to clamp onto an array of fibers for etching (2) translation stage to raise and lower the fibers to a specified height (3) USB microscope used to monitor the fibers during the etching process. All components are mounted onto on an optical breadboard for stability and portability.

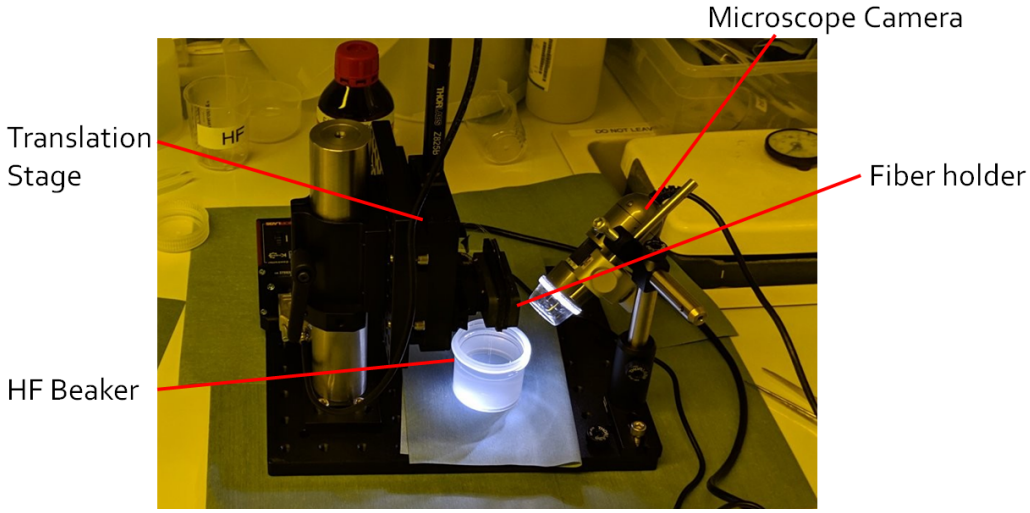

Figure 4.1: Overall setup used for acid etching of optical fiber.

The fiber holder consists of two sheets of rubber which have magnets stuck to them. The magnet on the bottom sheet of rubber is also adhered to a dovetail rail carrier which can be screwed on a dovetail rail on the translation stage. For each etching run, up to five fibers are arranged equidistant in an array on the bottom sheet of

rubber, using copper tape to hold them in place. Finally, the top rubber sheet is used to magnetically clamp the fibers firmly in place during etching.

The fibers used are Corning SMF-28e+ single-mode fibers with minimum attenuation at 1550 nm, coating diameter of 242 µm, cladding diameter of 125 µm, and core diameter of 8.2 µm [13]. The fibers were mounted with 5 cm of overhang from the holder and the coating was stripped from the last 1.5 cm of the fiber to expose the cladding.

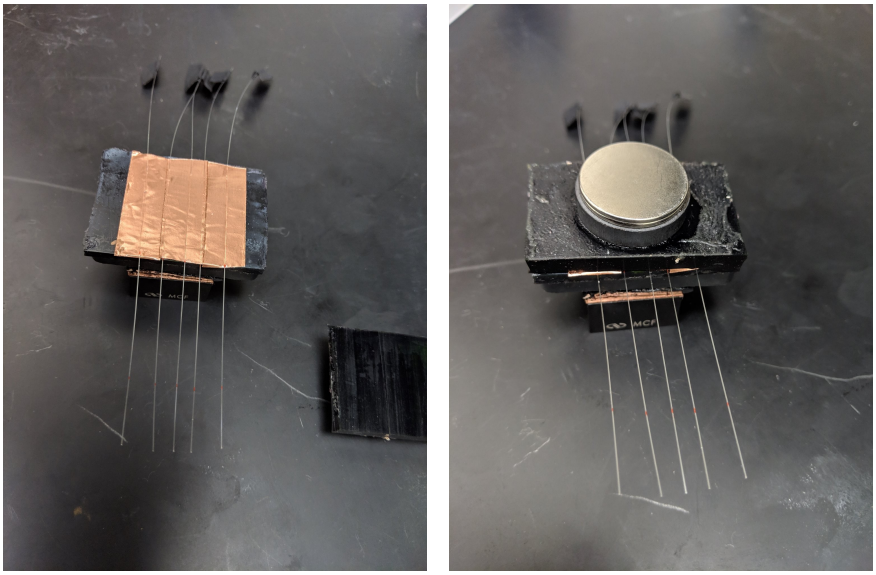

(a) Fibers arranged on the fiber holder and held in place using copper tape.

(b) Fibers clamped securely using magnets.

Figure 4.2: Fiber holder used to clamp the fibers during acid etching.

The fiber holder was clamped via a dovetail rail to a Thorlabs PT1-Z8 one-axis motorized translation stage which was driven by a Thorlabs KDC101 K-Cube brushed DC motor controller. The translation stage provides precise vertical positioning with repeatability ±1.0 µm with a travel range of 25 mm, allowing for accurate control of the fiber etching height and time.

In order to monitor the fiber during immersion into the HF, we used a Dino-Lite AM4113ZTL long-working distance USB microscope that provided a magnification of 90x at a distance of 4.66 cm. This long working distance was necessary since it is unsafe to place the microscope too close (~several mm for typical microscopes) to the surface of the HF.

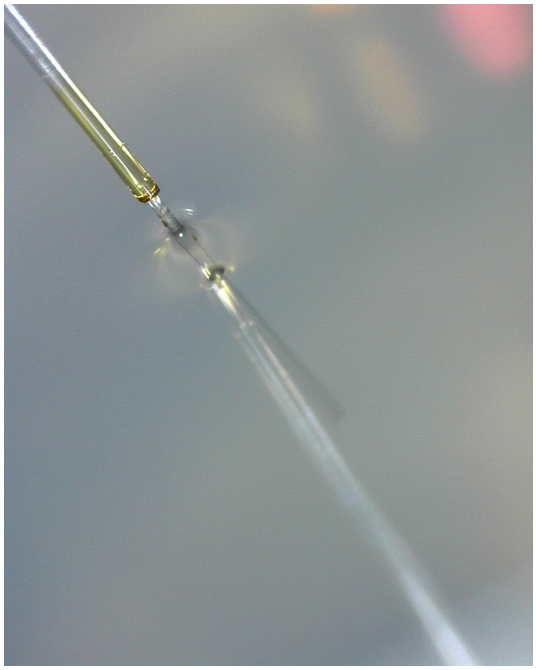

Figure 4.3: Close-up of a single optical fiber being immersed in HF during etching. The liquid air-interface as well as the point on the fiber where the coating has been stripped can be clearly seen.

Fig. 4.3 shows a sample photo taken by the Dino-Lite camera, with the fiber coming in from the top left and its reflection on the liquid surface coming in from the bottom right. The camera image allows us to clearly observe the height at which the fiber first enters the liquid surface and adjust the translation stage settings accordingly to maintain the same etch length across runs.

Etching procedure

The array of fibers, each with 1.5 cm of coating removed from the tip, is first dipped in an 80 ml solution of Cyantek Nano-Strip for 12 minutes, which consists of a mixture of sulfuric acid, peroxyonosulfuric acid, hydrogen peroxide, and water [47]. Nano-Strip can effectively react with organic compounds, helping to clean the surface of the fiber cladding of any remaining acrylate coating as well as any other impurities on the surface. The fibers are rinsed with deionized water after the Nano-Strip clean.

The etching process consists of two steps, with the first step involving HF (Macron Hydrofluoric Acid, 52%) and the second step involving buffered HF (Transene, Buffer HF Improved), which is a mixture of HF and NH_4F. It is advantageous to use these two different types of etchants as we can take advantage of the vastly different

etch rates in HF ($\approx$ 3.5 µm diameter min^{-1}) compared to buffered HF ($\approx$ 0.3 µm diameter min^{-1}). Therefore, we can first do a rough estimate of the etch time using HF, and then do fine adjustments of the final etch diameter in buffered HF without needing to control the etch time too precisely since the etch rate is much slower. Additionally, the relatively quick etch rates of HF tends to lead to surface roughness on the surface of the fiber which might cause scattering and power loss. Conversely, the slower etch rate of buffered HF will help to smooth out these bumps, leading to a surface that appears smooth on the scale of at least tens of nanometers.

For both steps, 40 ml of the respective etchant is added to a beaker followed by a layer of Sigma-Aldrich *o*-xylene. The layer of *o*-xylene is added dropwise using a disposable pipette until a complete layer is formed on top of the etchant (*o*-xylene is organic and is thus immiscible with the polar etchant), and then 5 additional drops are added to ensure that the layer of *o*-xylene remains even after any possible evaporation.

In the first etching step, the fibers are gradually lowered until the fiber tip reaches the *o*-xylene-HF interface. The vertical position on the translation stage at this point is noted, which we denote as x. The fibers are then lowered by another 3.5 mm and left at position $x - 3.5$ mm (positive coordinate indicating upwards) to be etched for 30 minutes. This thins the fiber from the cladding diameter of 125 µm to a typical diameter of approximately 10 µm. The length of this thin portion of the fiber is typically several mm. Following this, the fibers are raised using the translation stage by 2 mm to position $x - 1.5$ mm and etched for another 2 minutes. The part of the fiber that is still exposed to the HF during this 2 minutes is completely etched away, leaving behind a thin portion of fiber with length approximately 2 mm (since we raised the fiber by 2 mm).

Fig. 4.4 shows a close up of an array of 5 fibers being immersed in HF during the etching phase. The black portion on the fibers is the polymer cladding that reacted with the Nanostrip during the initial cleaning phase and plays no part in the taper formation process. After this etch in HF, the fibers are rinsed with deionized water and the etchant is replaced with buffered HF with a layer of *o*-xylene on the liquid surface. The fiber is lowered to position $x - 5.5$ mm, which is 2 mm lower than the etch height during the first HF etch. This gives us some margin of error to account for a possible difference in the liquid level for buffered HF compared to HF and ensures that the tapered portion from the HF etch lies completely within the buffered HF layer so that it can continue to be etched.

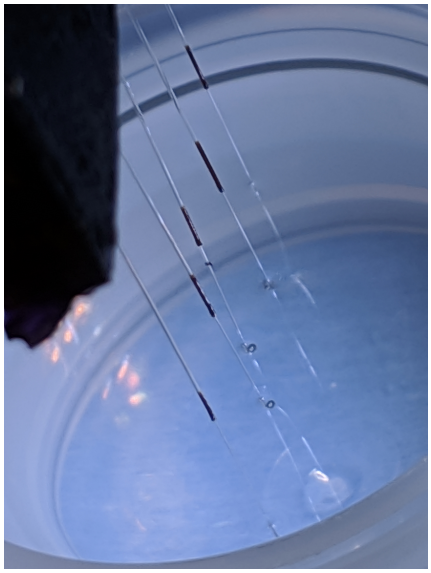

Figure 4.4: An array of five optical fibers being etched in HF.

The fiber is etched in buffered HF for approximately 50 minutes, although there is some deviation of this duration due to human error in timing during the initial HF etch. Since the measured rate of etching in HF is approximately 12 times that of the etch rate in buffered HF , a small etch time difference of 5 seconds in HF can translate to a difference of 1 minute in buffered HF. Starting from about 40 minutes after the start of the buffered HF etch, the fiber is periodically removed from the buffered HF, rinsed in deionized water, and observed under an optical microscope to determine when the fiber etch is complete. We terminate the buffered HF etching when the length of the fiber taper is approximately 300 µm or shorter.

Sample characterization

After the fiber etching has been completed, it can either be used for coupling light with a tapered waveguide, or it can be observed under a Nova 600 Scanning Electron Microscope (SEM) to determine its taper geometry and surface properties on a nanometer-level precision. In the former case, the fibers would be placed back onto the holder in Fig. 4.2 and stored until it is needed.

When preparing fibers for SEM, we stick them to a glass slide using copper tape, and coat the fiber with a 4 nm layer of carbon using a Leica EM ACE600 vacuum carbon coater. This layer of carbon is necessary to make the sample conductive and prevent charge buildup during SEM, but also affects the light propagation properties of the fiber and thus they can no longer be used for coupling experiments. Once fiber

etching procedure and timings were finalized, SEM images of several fibers made using the same procedure were taken to ensure that they had similar taper shapes, which gave us confidence that the fibers used for the coupling experiments also had the desired geometry despite not being observed under the SEM.

Fig. 4.5 shows a typical SEM of a tapered fiber with geometry similar to fibers eventually used in the coupling experiments.

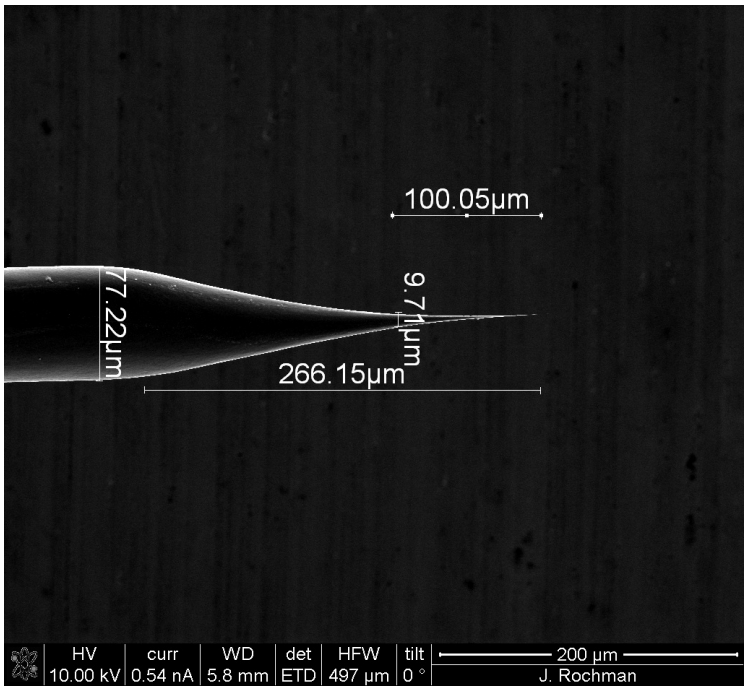

Figure 4.5: Typical SEM image of a fiber with taper parameters similar to those used in the actual coupling experiments.

4.2 Waveguide fabrication

The basic structure of the the waveguide involves a beam of silicon suspended above an air gap with photonic crystal mirror holes etched into it followed by a tapering of the waveguide width until some fixed minimum width. The waveguide is manufactured on a silion-on-insulator (SOI) wafer using electron-beam (e-beam) lithography to pattern the desired waveguide shape on a resist, which will then lead to selective removal of regions of the resist upon development. The structures on the resist drawn by the e-beam can then be transferred onto the layer of silicon through anisotropic etching.

Waveguide design

We show a typical AutoCAD design preview of the tapered waveguide in Fig. 4.6. In the AutoCAD design, we are able to freely adjust the values of the geometrical parameters, including the taper rate of the waveguide, the maximum waveguide width, and the location and sizes of the photonic crystal holes as well as the supports. We can then create arrays (typically 4×8) where we sweep over values of these parameters, since the designed dimensions may not correspond exactly to the actual fabricated outcome, especially for the photonic crystal hole sizes. Therefore, we need to insert a length bias in the designed dimensions in order to correct for these systematic errors. Another additional parameter that was of interest was the waveguide taper length, since a longer taper length was preferable as it led to higher transmittances in the simulations, but one possible concern was that they might have a higher propensity to be broken during the wet etching process. Therefore, arrays with different taper lengths were also designed to obtain statistics on this.

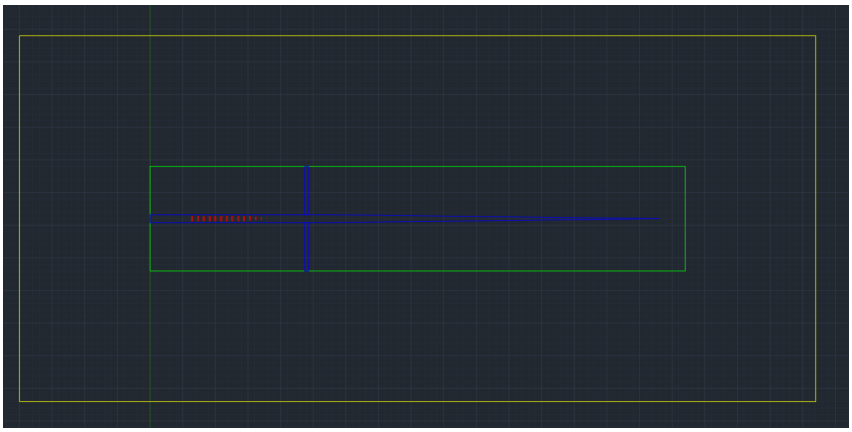

Figure 4.6: AutoCAD design for a typical tapered waveguide with various colors indicating various features of the structure.

The various colors refer to distinct layers in the geometry definition so that we have the option to indicate to the e-beam writing software, BEAMER [48], which regions should be irradiated with the electron beam. Here, the e-beam will be set to write between the yellow and green boxes as well as the region enclosed by the blue boundary but excluding the red holes. As we will be using a negative photoresist, the regions of the resist irradiated by the e-beam will become cross-linked and become resistant to dissolving in the developer. This protects the layer of silicon below it and prevents it from being etched away in a later step in the fabrication process. Thus, from the blue region, we will obtain a waveguide taper that is freely-suspended since its surroundings are not written by the e-beam.

There is a need to irradiate the e-beam in a border around the waveguide as shown by the yellow rectangle, because otherwise those regions would also be etched away and the freely-suspended waveguide would have no vertical surface to be attached to. The width of the border between the yellow and green rectangles are determined by the etch rate of the BHF in the last step of the fabrication process as shown in Fig. 4.7, since the SiO_2 layer under the top silicon layer would be etched away, leading to eventual undercutting of the top Si layer. Thus, if the border was designed to be too narrow, the underlying SiO_2 layer would be completely dissolved, causing waveguide to be washed away as it no longer has any supporting layer below it. In practice, this border was set to be 10 µm to prevent this from happening.

Fabrication procedure

We use a wafer of SOI with a buried oxide thickness of 3 µm and a top Si thickness of 500 nm. As our target waveguide height is 300 nm, we first need to thin the top Si layer. This is done by oxidation to create a top layer of oxide, followed by 5 minutes of acid etching in buffered HF to remove the oxide layer. A layer of HSQ resist is spun onto the wafer and baked. The waveguide design is patterned using e-beam lithography on a Raith EBPG 5200 using doses ranging from $600 \sim 900\,\mu C/cm^2$ for the box surrounding the waveguide and doses 1800 and $2000\,\mu C/cm^2$ for the waveguide itself. The chip is subsequently developed in 25% TMAH for 20 seconds. The pattern is then transferred onto the silicon layer using the pseudo-Bosch process in a SF_6/C_4F_8 plasma, where the SF_6 etches the silicon isotropically to form SiF_4 while the C_4F_8 passivates the sidewalls to allow for anisotropic etching of the silicon [49]. The wafer is etched in an Oxford III-V System 100 inductively coupled plasma reactive ion etching (ICP-RIE) etcher for 3 minutes 30 seconds. Finally, the layer of oxide is etched in 25 minutes of buffered HF, leaving behind undercut portions of the top silicon layer suspended above an air gap.

The fabrication process is summarized in Fig. 4.7, and a sample chip with waveguides fabricated on it is shown in Fig. 4.8 with the arrays of waveguides clearly visible. The dimensions of the chip shown is approximately 1 cm by 1 cm. In the last step of Fig. 4.7, the top layer of silicon is able to be suspended above an air gap because these suspended pieces are physically connected to other regions of silicon which still have the layer of SiO_2 below them for support.

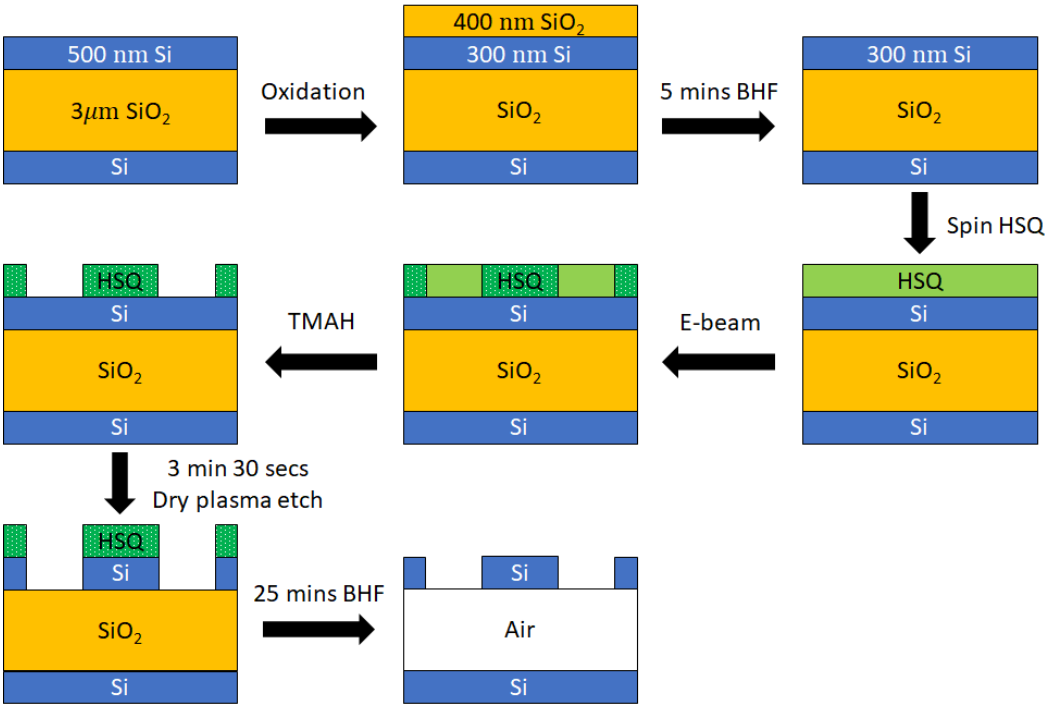

Figure 4.7: Fabrication procedure for the waveguide.

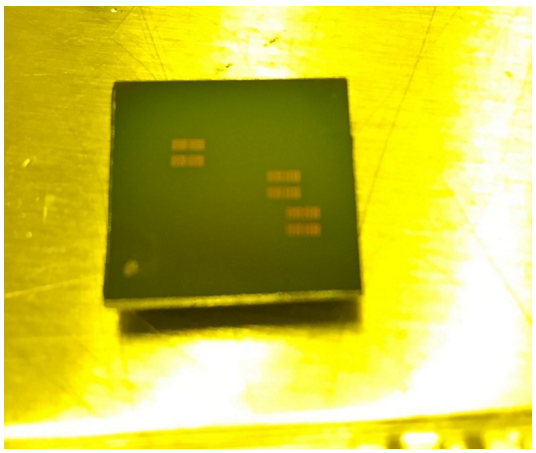

Figure 4.8: Typical wafer after waveguide fabrication. This wafer has 3 arrays of waveguides etched on it, each comprising of 64 separate copies of the waveguide.

Sample characterization

The fabricated waveguides can be characterized more closely under an SEM, and a sample SEM image is shown in Fig 4.9. The light regions are the top silicon layer while the dark regions are the underlying oxide layer. The image is taken at a 45-degree tilt to observe the thickness of the overhanging Si beam and to make sure that the silicon oxide layer beneath the top Si layer has indeed been etched away to

form a freely-suspended waveguide. The buried layer of silicon oxide is not directly visible but its edges can be seen as a bright glow under the border surrounding the tapered waveguide.

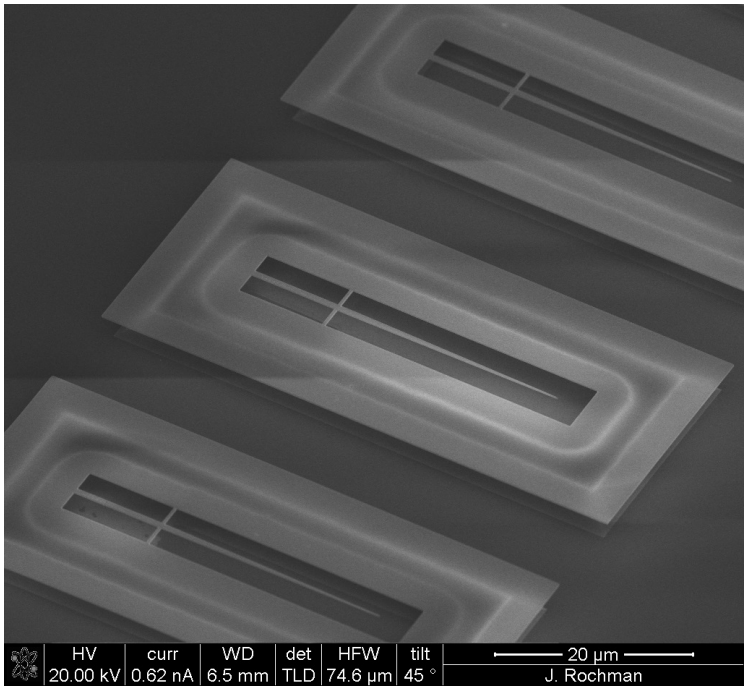

Figure 4.9: Typical image of an array of waveguides under an SEM. The photonic crystal holes are not visible in this image.

4.3 Fiber-waveguide coupling

This portion of the experimental setup combines the product of the previous two sections by measuring the transmission coupling between the tapered fiber and the tapered waveguide. We send light into the tapered fiber which couples into the waveguide where it reflects off the photonic crystal mirror back into the fiber and into a circulator which sends the signal to a photodidoe to be measured. A schematic of the optical coupling experiment is shown in Fig. 4.10.

The setup is relatively simple, with a JDS Uniphase OAB Optical Amplifier erbium-doped fiber amplifier (EDFA) sending in light at approximately 1550 nm into the fiber through a circulator. The non-tapered end of the fiber is spliced to a fiber optic connector for easy interfacing with other optical components (Fig. 4.11a). The tapered fiber is placed on top of a 3-axis rotation stage (Thorlabs TTR001) which is itself placed on top of a 3-axis Thorlabs MAX311D closed-loop piezoelectric translation stage for precise alignment of the tapered fiber onto the waveguide. The

rotation stage has a rotation angular resolution of $< \pm 0.04^\circ$ in all 3 axes while the piezoelectric stage when driven with an open loop drive has a theoretical resolution of 20 nm and a bidirectional repeatability of 200 nm. As discussed in section 3.2, we expect that we would require an axial positioning precision of about 10 µm and a transverse positioning precision of about 100 nm. Therefore, we expect that our high level of positioning precision as well as the numerous degrees of freedom is sufficient to allow us to precisely position the fiber onto the waveguide in order to maximize the coupling efficiency. The collected light from the circulator is detected using a Thorlabs S122C germanium photodiode power sensor.

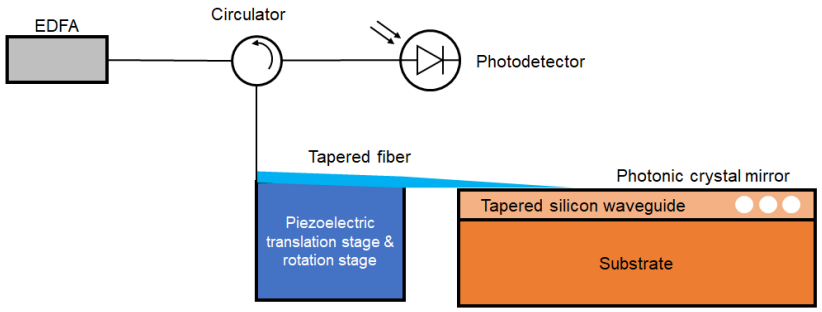

Figure 4.10: Schematic of optical coupling experiment. The silicon waveguide is tapered in the dimension going into the page and has a constant thickness, and thus appears as a rectangle here.

In order to align the fiber properly with the waveguide, the waveguide is observed using a confocal microscope setup (Fig. 4.11b) with an LCPLN50XIR objective lens which has a magnification of 50x and provides a field of field of approximately 80 um. A sample image of a tapered waveguide and its supports under the confocal microscope is shown in Fig. 4.11c, which shows that we can clearly distinguish features whose lengths are on the order of several hundred nanometers (for scale, the waveguide width is 600 nm). The image is focused into both an optical and IR CCD, which allows us to monitor both frequencies simultaneously. At the same time, the side view of the fiber is monitored using a USB camera to vertically align the fiber and check that it is indeed touching the waveguide chip (Fig. 4.11d).

The alignment procedure is done by first tilting the fiber downward as much as possible using the rotation stage, and then using the piezoelectric stage to lower the fiber in the z-direction until it appears to be in the same focusing plane as the waveguide, which indicates that it is indeed at the same z height. The fiber is then shifted around in the x (transverse) direction using the piezoelectric stage while being observed under the confocal microscope until it appears aligned with the

waveguide's symmetry axis. Finally, the fiber is moved in the y (axial) direction and we observe for any changes in the power meter reading.

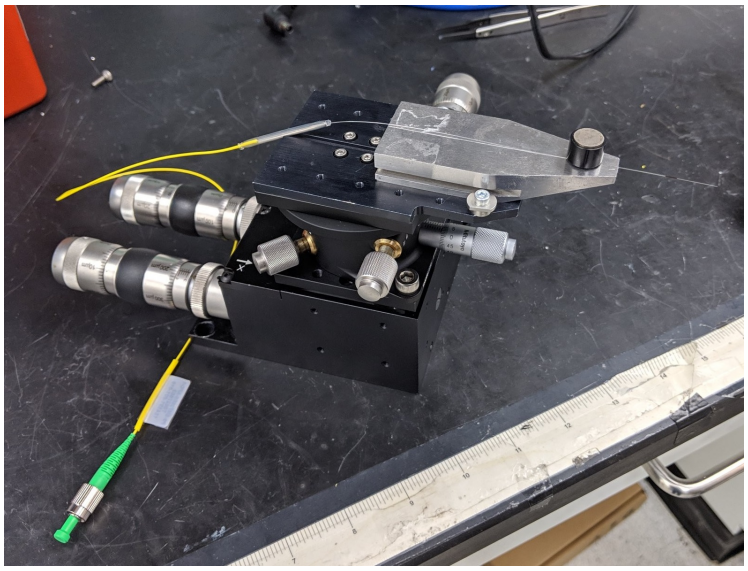

(a) Fiber mount placed on top of rotation stage and piezoelectric translation stage. The non-tapered end of the fiber is spliced to a fiber connector and connected to an EDFA.

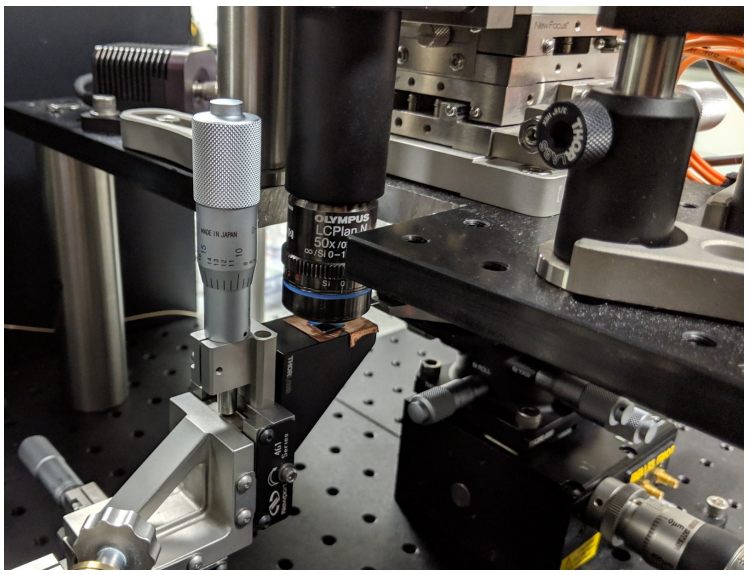

(b) Fiber aligned with the waveguide wafer chip under the confocal microscope.

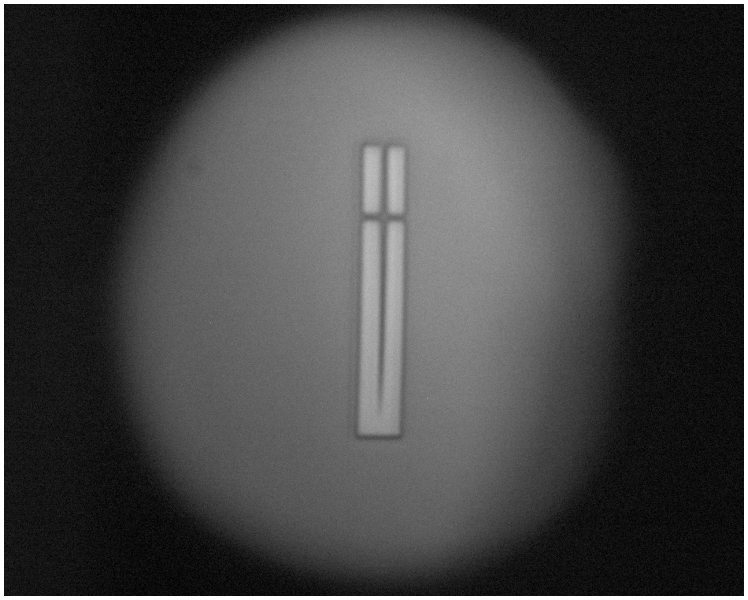

(c) View of a tapered waveguide under the confocal microscope. The field of view is approximately 80 µm by 80 µm.

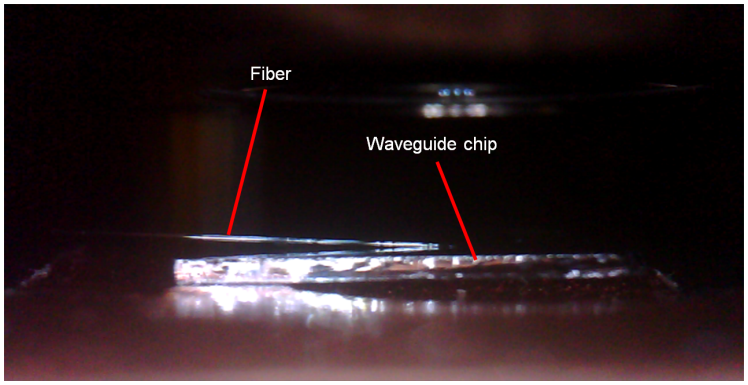

(d) Side view of the fiber aligned with the waveguide wafer.

Figure 4.11: Fiber coupling setup.

Chapter 5

EXPERIMENTAL MEASUREMENTS & RESULTS

In this chapter, I present a characterization of the geometry of the fabricated fiber and waveguide tapers and show that they are indeed mostly in line with our design parameters from Chapter 3. Following that, I discuss the results of the actual fiber-waveguide coupling measurements and suggest points for improving the coupling efficiency in the future.

5.1 Fiber geometry characterization

Fiber taper geometry

As mentioned in the fiber etch procedures (section 4.1), each fiber is first etched for 30 minutes in HF and then raised vertically by 2 mm where the etch is continued for another 2 minutes. The fiber is then lowered by 4 mm and etched for 40 minutes in buffered HF. Finally, we periodically observe the fiber under an optical microscope to determine if the etch is complete, and return it to the buffered HF for additional etching if necessary. Fig. 5.1 shows a comparison under the optical microscope between a fiber that we deemed were under-etched and one that we deemed was suitable for our usage.

Fig. 5.1a shows a fiber at 10x zoom under an optical microscope showing a visibly long and thin "tail" at the fiber tip of length on the order of a millimeter. The visual characteristics of this tail is a high aspect-ratio region (long and narrow) where the fiber diameter is small and constant (i.e. does not have any significant taper). On the other hand, adding more time to the buffered HF etch gives rise to the fiber in Fig. 5.1b (taken at twice the magnification, 20x), where we can see that most of the tail has been etched away and that the fiber terminates soon after the fiber stops tapering and the taper angle goes to zero.

A series of SEM images for a tapered fiber that we fabricated is shown in Fig. 5.2. The fiber was etched in 32 minutes of HF as described in section 4.1 followed by 44 minutes of buffered HF.

The top left image (Fig. 5.2a) shows the overall view of the entire fiber taper, starting from the initial cladding diameter of 103 μm all the way to the fiber taper tip. While the nominal specifications of the cladding diameter is 125.0 ± 0.7 μm

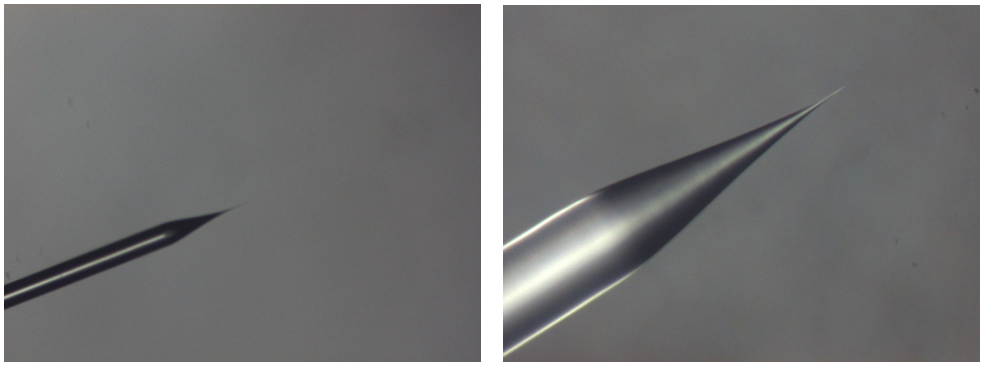

(a) Fiber after 32 mins HF and 48 mins buffered HF at 10x zoom. Visible long thin taper portion at fiber tip can be seen.

(b) Fiber after 32 mins HF and 53 mins 15 seconds buffered HF at 20x zoom. Most of the long thin taper has been etched away

Figure 5.1: Optical microscope view of tapered fiber at different etch times, showing how the end of the etch was determined by observing whether the long and thin taper portion at the fiber tip was present.

[13], this smaller cladding diameter is likely due to either overstripping by the fiber stripper when stripping away the outer coating of the fiber, or it has been gradually thinned by HF vapor present from HF liquid evaporating during the etching process. The entire taper is approximately 200 µm long, and we measure an initial taper-half angle of 12.5° for this initial portion of the fiber.

Even though these values might seem wildly different from our design parameters of 2° half-angle with taper length 25.8 µm, this is not an issue, because here were are merely thinning away the cladding surrounding the core, which has diameter 8.2 µm. Thus, the light is still entirely being guided within the core which is unaffected at this point, and thus the much faster taper rate would not lead to to any loss of guided optical power.

In our simulations, the design taper length of 25.8 µm was supposed to be measured starting from the point where the fiber had radius 1 µm. Thus, in Fig. 5.2b, we zoom into the tip regions of the fiber and measure the length starting from the point where the fiber has radius 1 µm, and indeed we see a tapered length of 28.65 µm which is very close to our design parameters. Moreover, we can measure the taper half-angle at the fiber tip in Fig. 5.2c and see obtain a value of 2.1°, which is once again in good agreement with what we demanded from our theoretical model. The fact that the taper angle decreases along the fiber can be explained by the fact that we started with HF and switched to buffered HF which has an etch rate almost 12 times

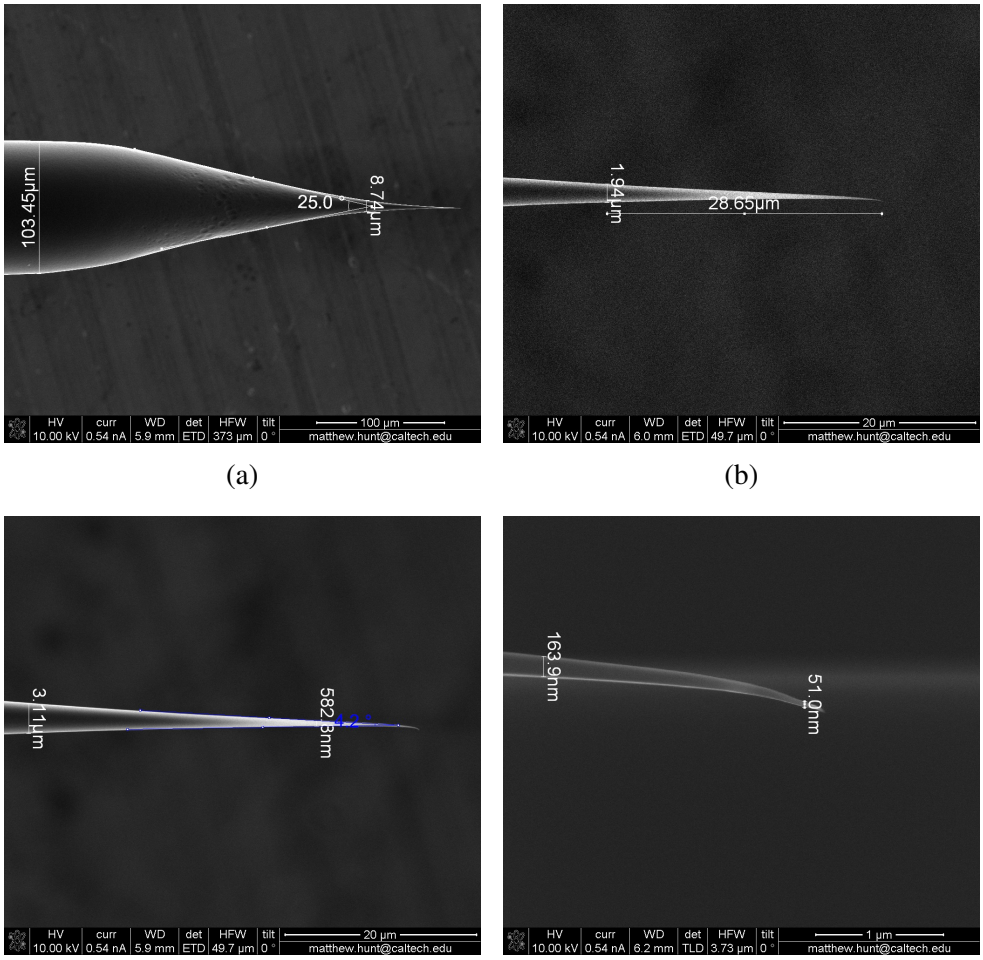

(a) (b)

(c) (d)

Figure 5.2: SEM view of tapered fiber at various magnifications. The fiber was etched using 32 mins of HF and 44 minutes of buffered HF.

smaller, and thus the taper angle produced by buffered HF should also be smaller.

Finally, we observe the diameter of the fiber at the tip, which we measure to be approximately 51 nm. We find that the fiber tip diameter varies somewhat between fibers, but typically lies between 50 nm and 200 nm. This value of 51 nm somewhat smaller than our simulated minimum diameter of 200 nm, but we believe this should not lead to any significant impact on the light coupling and field distribution. This is because when the fiber is much smaller than the width of the waveguide below it, most of the field intensity will be concentrated within the waveguide, with the fiber having minimal impact on the mode index and field distribution. An illustration can be seen in the right hand side mode in 3.7.

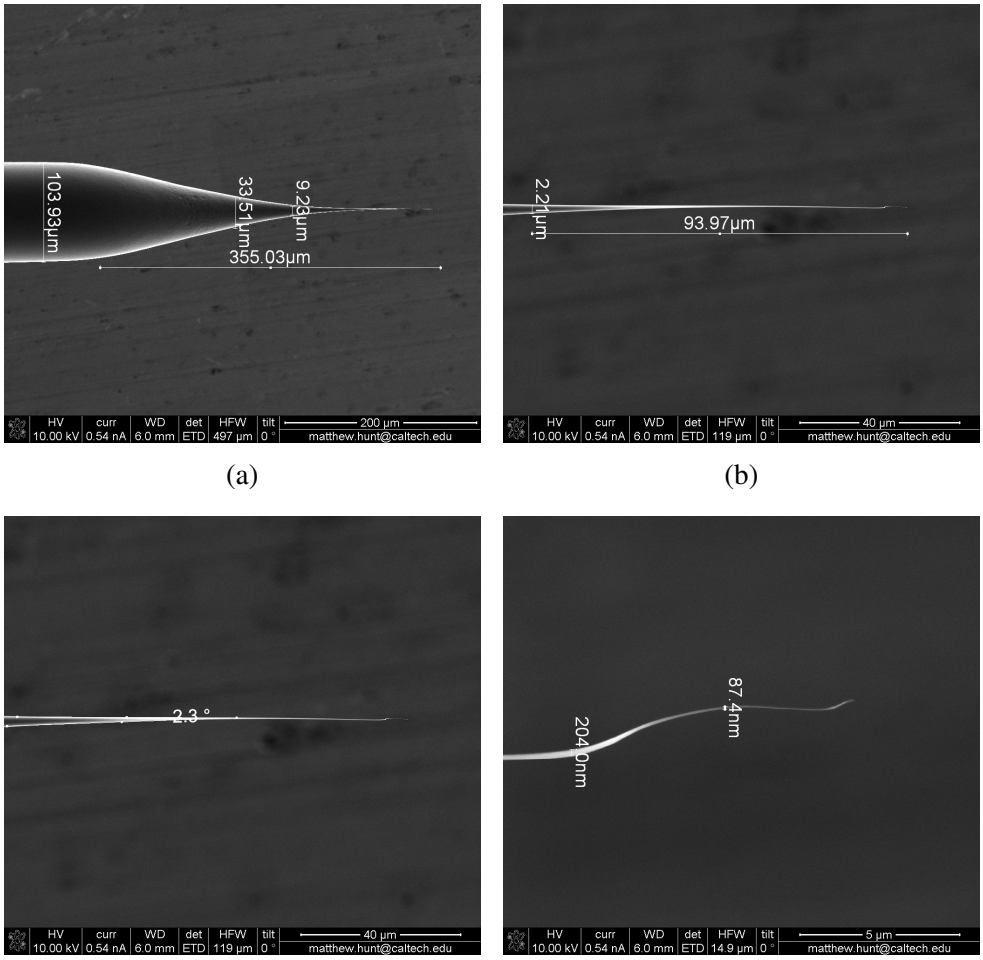

Figure 5.3: SEM view of tapered fiber with overly long taper. Fiber was etched in the same run as the one in Fig. 5.2 but only had 42 mins etch in buffered HF instead of 44 mins.

As an illustration of a fiber which is under-etched and thus has an overly long taper, we show in Fig. 5.3 the SEM images of a fiber which was etched in the same experimental run as the one in Fig. 5.2 but had 2 minutes less of buffered HF etch time. First of all, we immediately see in Fig. 5.3a that the length scale is double that of Fig. 5.2a, and our overall taper length is 355 µm with a visibly long "tail" at the fiber tip. Moreover, if we measure the fiber taper length starting from the point with radius 1 µm to the tip (Fig. 5.3d), we obtain a length of about 90 µm, which is more than 3 times the designed length from the simulations. It turns out that the taper half-angle (Fig. 5.3c) is also somewhat smaller at 1.15°, which is consistent with the longer taper length. Looking more closely at the fiber tip reveals

an unusual geometry that we believe is due to mechanical stresses bending the extremely narrow fiber tip. While we were unable to measure the exact tip geometry due to the difficulty in focusing onto the narrow fiber tip, we estimate that it should be approximately 50 nm or less. These images illustrate our reason for deciding to not use fibers with excessively long "tails" – they have a higher propensity to break, bend or swing around due to airflow and mechanical stresses, and alignment of a long and flimsy taper would be more difficult compared to a shorter one.

Surface roughness

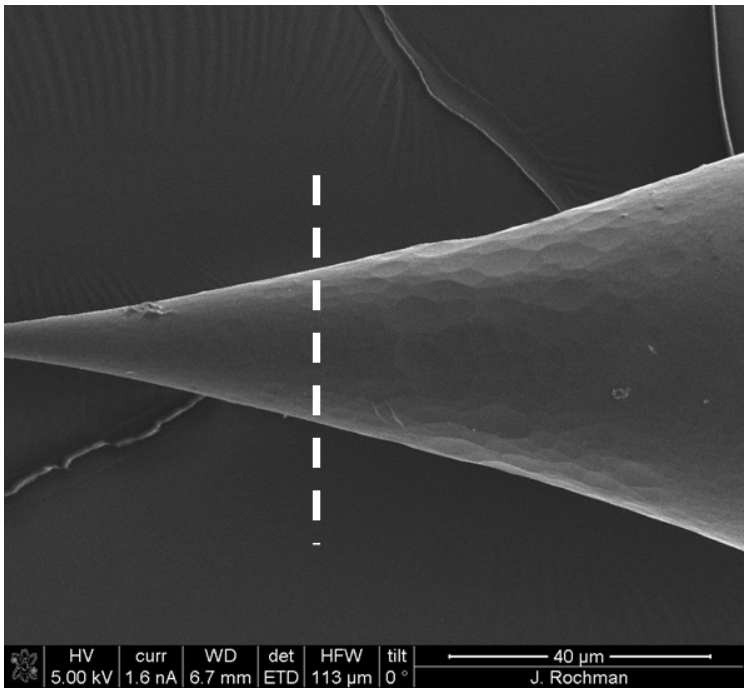

Figure 5.4: Illustration of surface roughness on fiber caused by HF compared to buffered HF. The dotted white line indicates the boundary between parts of the fiber that were exposed to only HF and parts that were exposed to buffered HF after HF.

Finally, we also briefly address some potential concerns with regards to surface roughness due to the wet etching process [43], as remnant HF often clings onto the fiber surface and causes small amounts of additional etching at random points on the surface even after the fiber has been removed from the HF beaker. This might be a problem as these features could lead to scattering of the light guided by the fiber and greatly decrease coupling efficiencies if they are on the order of a wavelength.

Fig. 5.4 shows a comparison of a portion of the fiber where the part right of the white line was exposed to only HF while the part on the left was additionally etched with buffered HF after the initial HF etch. We see a clear difference in surface smoothness

at this interface, indicating that HF by itself is indeed insufficient to achieve a smooth etch surface. Moreover, the dents and bumps on the right side have length scales on the order of $5 \sim 10\,\mu$m, which is much larger than the wavelength of the light (1535 nm) and thus would lead to power losses. The smooth surfaces of the fiber can also be ascertained in the images of the fiber tips in the figures above, which are take at much higher magnification levels and still show no indications of roughness.

5.2 Waveguide geometry characterization

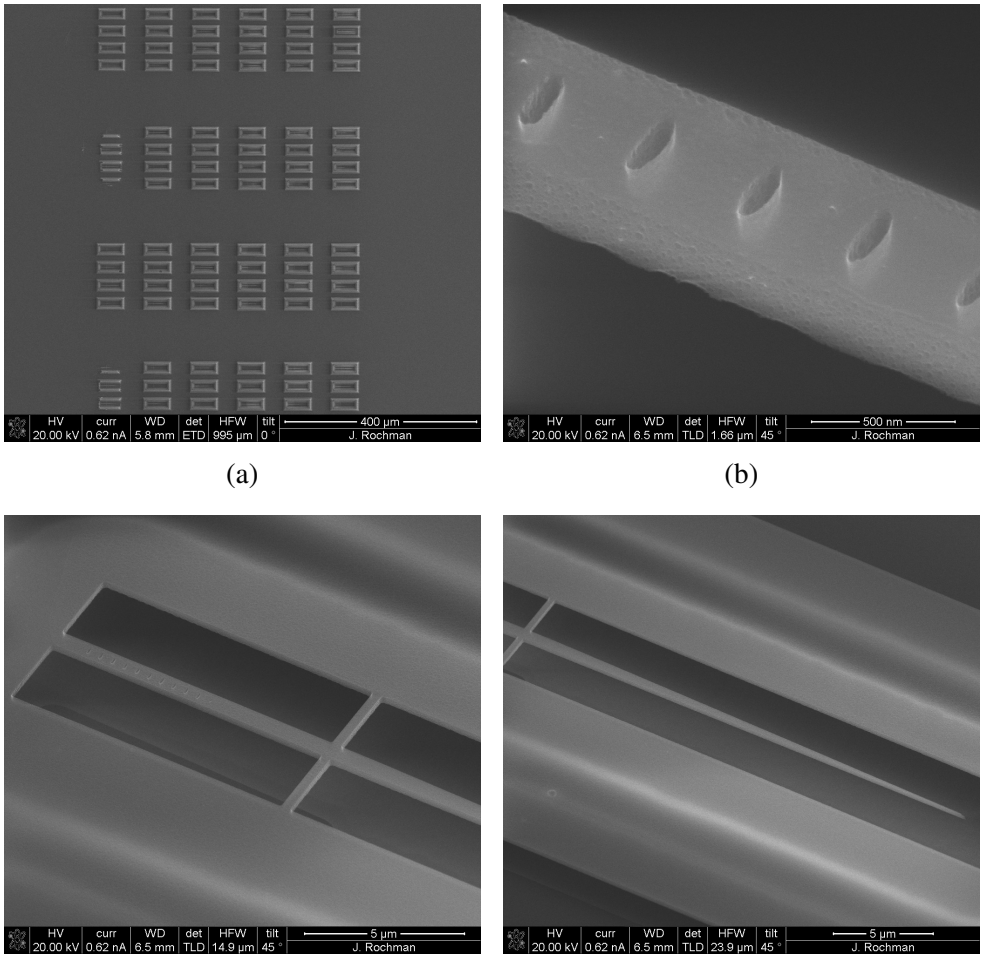

Figure 5.5: SEM images of fabricated tapered waveguides, showing an array of waveguides with different biases for the holes sizes and different e-beam doses for the surrounding border, as well as a close-up of the photonic crystal mirror holes and the overall view of the waveguide.

Fig. 5.5 shows the SEM images taken of the fabricated tapered waveguides. An array of waveguides is shown in Fig. 5.5a, where each column represents a different e-

beam dose for the border surrounding the waveguide, going from 400 $\mu C/cm^2$ in the leftmost column (not present in the image as the dose was too low) to 1000 $\mu C/cm^2$ in the rightmost column in steps of 100 $\mu C/cm^2$. The e-beam dose for the waveguide taper itself was fixed at 1800 $\mu C/cm^2$ for this image. The array is also arranged into 4 sub-arrays. The second and fourth sub-array from the top have proximity error correction (PEC) applied to them for the border e-beam dose, which we will discuss later. The third and fourth sub-array from the top have a slightly different geometry where the surrounding border was 1 μm further away from the waveguide compared to the first two sub-arrays' geometry. Finally, each row in a sub-array represents a different value for the size bias that we input for the photonic crystal hole sizes to account for any systematic errors in the e-beam patterning, such as due to dosages from nearby patches inadvertently increasing the dose surrounding the holes and changing the hole sizes. The size of these biases were from 10 nm to 25 nm in steps of 5 nm.

An image of an entire waveguide can be seen in Figs. 5.5c and 5.5d, where the images were taken at a 45° tilt to better observe the cross-sectional thicknesses of the top silicon layer. We can see that the waveguide does indeed have a photonic crystal mirror patterned into it, is supported by two support beams that connect it to the surrounding silicon border, and ends in a narrow taper. The waveguide also appears indeed be freely suspended in air with the layer of silicon oxide that was originally below it being fully etched away during the final fabrication step in buffered HF. A cross-sectional measurement of the top silicon layer gives a thickness of 259 nm, which is close to the expected thickness of 300 nm. The waveguide width was measured to be 572 nm, the waveguide tip width was 36 nm and the support beam width was 314 nm, all of which agree well with the designed geometry.

Taking a closer look at the waveguide and photonic crystal mirror holes in Fig. 5.5b, we see that the holes are indeed patterned into the waveguide and appear to penetrate through most of the waveguide's thickness. However, the holes themselves appear to have somewhat rough edges and have some distortion from being a perfect ellipse. Moreover, the waveguide itself appears to have some nanoscale roughness on the order of tens of nanometers, but we believe this should not affect the efficiency significantly as it is much less than the light wavelength. A more serious problem, however, is the measured hole size, which we find to be 264 nm by 100 nm for the major and minor axes of the ellipse with a variation of about 5 $\sim$ 10 nm between holes in the same waveguide. Unlike the other parameters that we measured so

far, this is significantly different from the designed hole shape of 400 nm × 130 nm (Table 3.1), and we expect that this will significantly degrade the performance of the photonic crystal mirror since the band structure would have changed greatly and we would no longer have a band gap at 1535 nm.

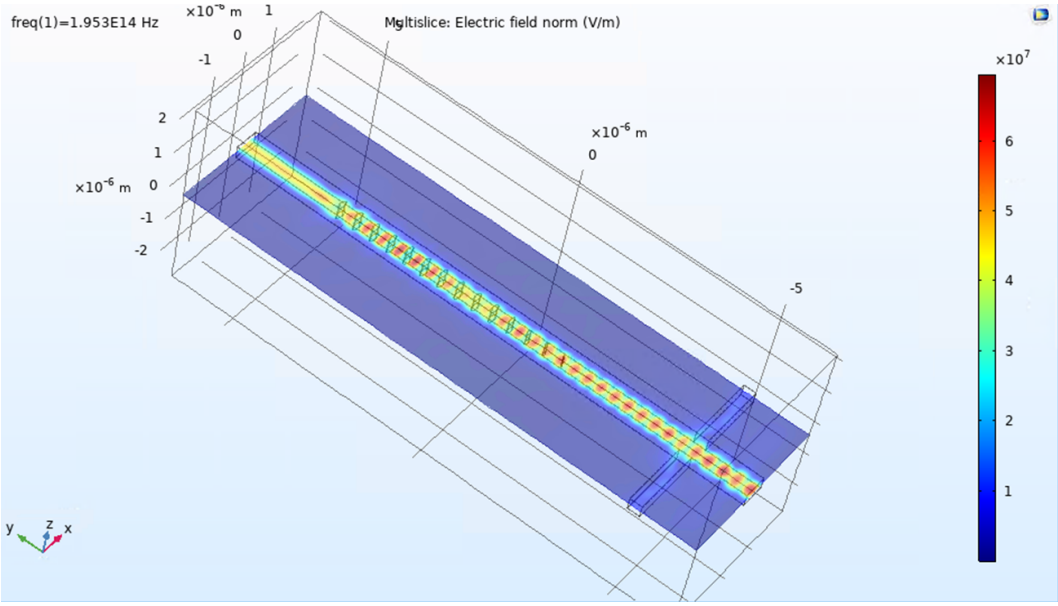

Figure 5.6: Reflection simulation of photonic crystal with actual fabricated hole sizes of 264 nm by 100 nm. We see that there is very low reflection with most of the light transmitting through as the hole size no longer creates a band gap at the light frequency.

Indeed, when we redo our simulation in Fig. 5.6, we see that this smaller hole size gives us a greatly degraded reflectance performance, with most of the light transmitting straight through as we no longer have a band gap at the light frequency. We obtain from this simulation a reflectance of 0.0538, transmittance of 0.787, and an absorbance and scattering of 0.159, which is to be compared with the expected reflectance of 0.842 in our theoretical design in Table 3.1. Because of this greatly reduced reflectance, the amount of reflected power collected from the fiber will also be correspondingly reduced. One point of note is that this does not affect the intrinsic coupling efficiency of our fiber-waveguide interface in any way, but only makes the reflected signal for our coupling efficiency measurements smaller and thus more difficult to detect.

Electron beam dose and proximity effect

We believe that the primary reason behind the hole sizes that are smaller than expected, as well as possibly the rough edges, is an effect known as the proximity

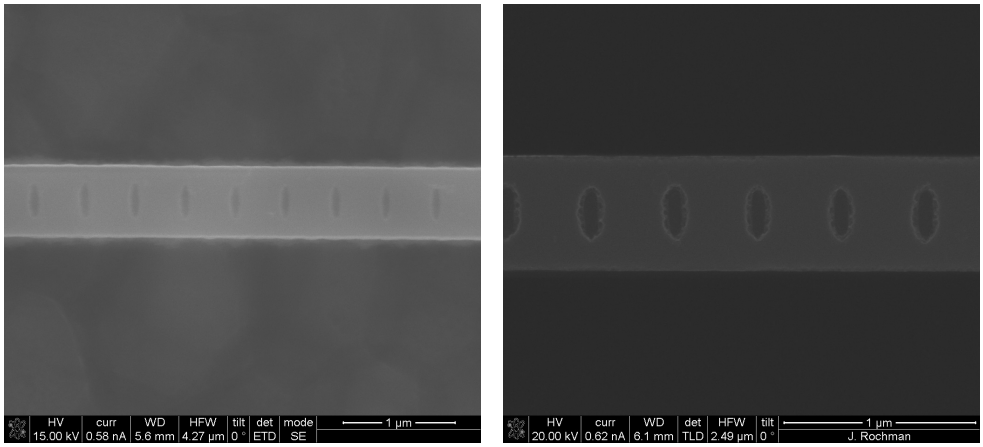

(a) Holes patterned using a dose of $800\,\mu C/cm^2$ (with PEC) for the surrounding border, showing that the holes are only partially etched through.

(b) Holes patterned using a dose of $600\,\mu C/cm^2$ (with PEC) for the surrounding border, showing fully etched holes but with rough edges.

Figure 5.7: Comparison of beam dose on photonic crystal holes.

effect [50], whereby an electron-beam causes non-zero doses in regions that are outside of the area being illuminated. This is due to the fact that when electrons from the e-beam impact the surface, they do not immediately get stopped at the surface of the resist, but instead typically penetrate $10 \sim 100\,\mu m$ into the substrate. There, they interact with the atoms in the substrate as well as backscatter from atomic nuclei, sending a scatter of lower-energy electrons in a broadened beam back towards the top layer of resist. These low-energy electrons then interact with the resist, causing exposure and cross-linking of the resist molecules in regions that might be far away from the initial beam location.

This proximity effect therefore leads to a complicated problem where e-beam patterning of one location affects the dose needed at another location. If we have too much background dose in the region where we expect to have holes, the resist in the holes will be cross-linked by the background dose, meaning that they will not be washed away by the developer, and thus the holes produced will be smaller than expected or holes might not even be fully formed at all. In order to partially account for this proximity effect, the BEAMER software that we use for controlling the exposure has an option for Proximity Effect Correction (PEC), which we apply in some of our fabrication tests.

An example of holes not being fully formed is demonstrated in Fig. 5.7a, which had a dose of $800\,\mu C/cm^2$ (with PEC) for the border surrounding the waveguide. We

can see that the holes are much smaller than they are designed to be and the color contrast of the holes compared to the surrounding waveguide is also relatively weak, indicating that the holes did not form fully through the entire depth of the waveguide. In contrast, a slightly better outcome is shown in Fig. 5.7b, which was made using a dose of 600 $\mu C/cm^2$ (with PEC). We see fully-etched holes that are somewhat closer to the designed hole size, but we still obtain a size of 264 nm $\times$ 100 nm compared to the target of 400 nm $\times$ 130 nm.

An important target in the near future would therefore be to further experiment with the e-beam dosage in order to accurately obtain the desired hole sizes with smooth edges. As we saw in Fig. 5.5a, doses below 500 $\mu C/cm^2$ give rise to borders that are either partially formed or are completely etched away during the wet etching step, and thus this sets a practical lower bound on the dose that we can set for the border. Other possibilities include lowering the waveguide taper region's dose, or by modifying the spacing of the border from the waveguide such that they are physically further apart.

5.3 Coupling efficiency measurements

Fiber observations

As a preliminary test of the tapered fiber's applicability for coupling with a tapered waveguide, a single tapered fiber was placed under the confocal microscope setup without a waveguide. Light from an EDFA was then sent into the fiber via the other end of the fiber taper which was spliced to a fiber connector. The EDFA light was attenuated by 10 dB before being sent into the fiber to avoid oversaturated images. The results are shown in Fig. 5.8, where the left column shows the optical images (illuminated using a white light LED) and the right column shows the infrared images (illuminated only using light scattered from the fiber itself). The fiber is moved vertically upwards in the series of images so that we can observe various parts of the fiber. In the bottom two images, we are seeing the parts of the fiber when it is still relatively thick; we observe little to no IR light leaking from the fiber, as evidenced by lack of bright spots on the fiber despite enhancing the brightness. This indicates that our taper is gradual enough and our fiber surface is also smooth enough that we do not have large losses from scattering off the fiber surface. Looking closer to the tip, we start to see bright patches near the fiber tip, which makes sense since the fiber starts getting narrower and narrower and loses its ability to support the propagation of the light in the fundamental mode, causing the light to couple out into the air and observed as bright areas. Finally, there is also a distinct bright spot

located at the tip of the fiber as the remaining light propagating in the fiber escapes from the fiber at the tip.

At the same time of taking these images, we also connected the fiber to a circulator which was then connected to a photodetector to measure if there was any inherent reflectance of the fiber when suspended in air. Over a 1 minute measurement period, we observed a mean reflected power of $3.367 \pm 0.066\,\mu W$ with the EDFA off and $3.374 \pm 0.066\,\mu W$ with the EDFA on. This indicated that there was no significant reflection from the fiber-air interface, which is a good indication that we would not experience additional power losses due to light reflecting off the fiber tip when we try to couple to the waveguide.

Fiber-waveguide coupling imaging

Finally, in order to measure the fiber-waveguide coupling efficiency, we place a tapered fiber near a tapered waveguide and do fine adjustments on the angle of the fiber until it was touching the waveguide surface. This was verified by checking that both the fiber and waveguide could be placed in focus at the same time, and thus they were located at the same vertical height. At the same time, once the fiber is touching the waveguide surface, it experiences adhesion forces that makes it go through a stick-slip motion when it is moved about on the surface. We therefore look out for these two observations to verify that the fiber is in contact with the silicon surface. At the same time, the position of the fiber was adjusted using the piezoelectric stage and the manual adjustment knobs until it was axially aligned with the waveguide and its tip was located along the waveguide taper, which was the optimal geometry determined from the simulations.

We show the observations in the infrared camera in the middle and right images in Fig. 5.9, where the incoming light is also 10 dB-attenuated. The middle image is an IR image of the waveguide with a fiber aligned onto it, where we also turn on the white light source (which is typically used for the visible light camera) in order to compare the bright spots in the infrared wavelength with the shape of the waveguide and its surrounding borders. The right image is the identical setup but with the white light source turned off so that the only light comes from the EDFA coupled into the fiber. The most apparent observation that we can make from the right image is the presence of multiple bright spots of scattering, which we can compare with the middle image to realize that the scattering occurs at the waveguide support beams as well as on the front and back walls of the border of silicon surrounding

the waveguide. A clearer image is shown on the left, where we show an optical microscope image of the waveguide together with the surfaces that we believe the IR light is scattering off shown in yellow.

We believe that we are observing scattering at these points on the waveguide because they are all vertical surfaces which can scatter any incoming IR light coming from the fiber. Therefore, we believe that the incoming light from the fiber is simply acting like a flashlight and shining IR light all over the waveguide (similar to the first 3 rows in Fig. 5.8), and then these vertical surfaces are acting as scattering surfaces that scatter light into our objective lens. This interpretation is supported by the fact that we stop observing these bright spots once we move the fiber too far forward or backward, and we observe a maximum scattering brightness when the tapered region that was shining brightly in Fig. 5.8 was placed near these vertical surfaces. This interpretation of the observed images means that we are not achieving the optimum alignment of the fiber with the waveguide, because most of the light from the fiber is being coupled out into the air and lost instead of going into the waveguide, and suggests that we should continue to tune the alignment of the fiber.

Upon achieving the optimal alignment, in theory we should not see any bright spots anywhere on the waveguide since almost all of the power should be reflected and relatively little should be scattered. However, there is another obstacle that we face in our current experimental setup, namely the fact that our fabricated photonic crystal mirror holes turned out smaller and rougher than expected in the e-beam lithography process. As a result, instead of achieving almost perfect reflection, we expect to observe some amount of scattering and transmission through our crystal instead, and we can use this disadvantage as a resource to help us verify whether our fiber is indeed making contact with the waveguide. As can be seen in the right image in Fig. 5.9, we do indeed observe some bright spots in the region along the waveguide where the photonic crystal holes are, as indicated by the red arrows. This suggests that our fiber is indeed coupling some amount of light into the waveguide, but this proportion is likely to be small and could be improved by improving the alignment. Moreover, these bright spots are unlikely to be due to simple scattering like what we observe for the other vertical surfaces, because these bright patches in the mirror region appear to be much more sensitive to the fiber alignment and disappear when the fiber is slightly shifted even when the other bright spots remain.

Fiber-waveguide coupling efficiency

Following the result of repeated adjustments to the alignment of the fiber, we were unfortunately unable to achieve a stable alignment of the fiber which gave rise to detectable signals on the photodetector measuring the power reflected from the fiber. However, while doing a manual scan of fiber position across the waveguide, we obtained several isolated spikes in the detected reflected power. As we simulated in Fig. 3.10, the transmitted power between the interface drops off rapidly when the fiber is several hundreds of nm off-axis, giving rise to a tight tolerance in the fiber's transverse position. Therefore, this measured spike in reflectance was likely a result of the fiber moving across the optimal coupling location. This caused a rapid rise in transmittance into the waveguide and followed by an equally quick drop in transmittance as the fiber moved off-axis. Subsequent attempts to replicate the power spikes by scanning the fiber over a similar location in space were unsuccessful.

In one case, we observed a peak reflected power 6.7 µW with a background noise floor of 2.8 µW, while in another case we observed a reflectance peak power of 10.0 µW with a background noise of 2.9 µW. While these are only isolated data points, we can use them as a lower bound on our coupling efficiency between the fiber and waveguide. From section 5.2, we estimate that the reflectance off the photonic crystal mirror should be $R = 0.0538$, and we can directly measure the power of the incoming EDFA light to be $P_i = 10.1$ mW. Denoting the efficiency of the fiber-waveguide coupling interface to be η, we have the following expression:

$$P_r = P_i R \eta^2$$

where η is squared since the light passes through the interface a second time when it gets reflected back into the fiber. We take P_r to be 10.0 µW − 2.9 µW = 7.1 µW after subtracting off the background power level. Plugging in the values:

$$\eta = \sqrt{\frac{P_r}{P_i R}} = \sqrt{\frac{7.1 \times 10^{-6}}{\left(10.1 \times 10^{-3}\right)\left(0.0538\right)}} = 0.114$$

We have therefore demonstrated a coupling efficiency of at least 11.4% using our tapered-fiber technique.

We can identify two main factors for this fiber performing not as well as expected. The first is our poor alignment of the fiber with the waveguide, leading to incomplete transfer of power into the waveguide. As demonstrated in Fig. 5.9, we see a large amount of scattering at various points on the waveguide, which indicates that we

are losing a significant amount of power to scattering instead of being directed into the waveguide. In the ideal case from simulations, when the fiber is optimally aligned with the waveguide, the light would be almost fully confined within the fiber and waveguides, and we should observe almost no scattered light. The second factor is likely due to the rough surface of the holes, which were not modeled in the simulation in Fig. 5.6. The hole roughness could further degrade the reflectance R, and make the actual value smaller than the value which we obtained.

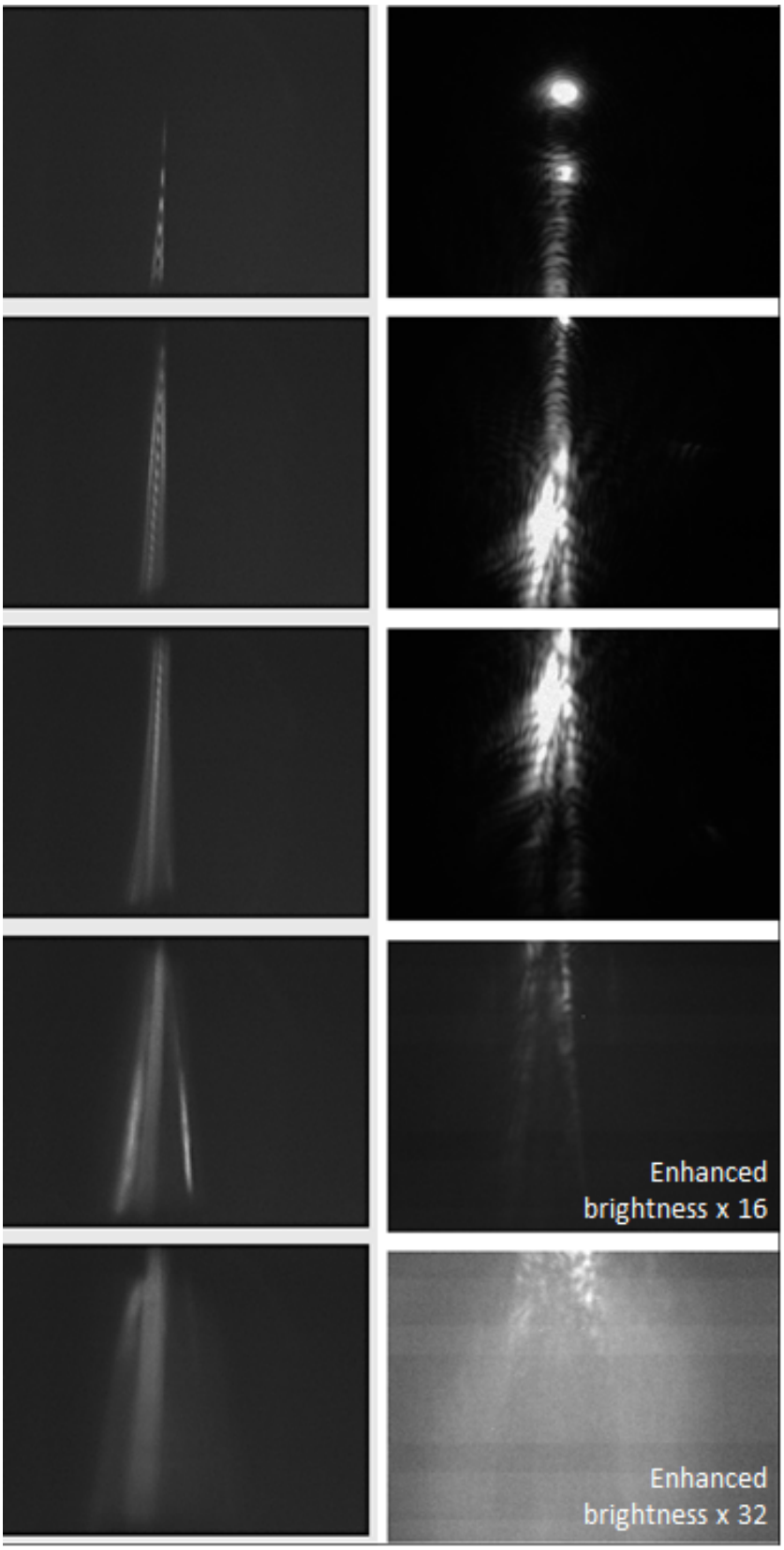

Figure 5.8: Optical (left) and IR (right) images of tapered fiber with EDFA light sent through it. The fiber is moved vertically upwards to observe various portions of the fiber. The bottom two IR images have their brightness enhanced for clarity.

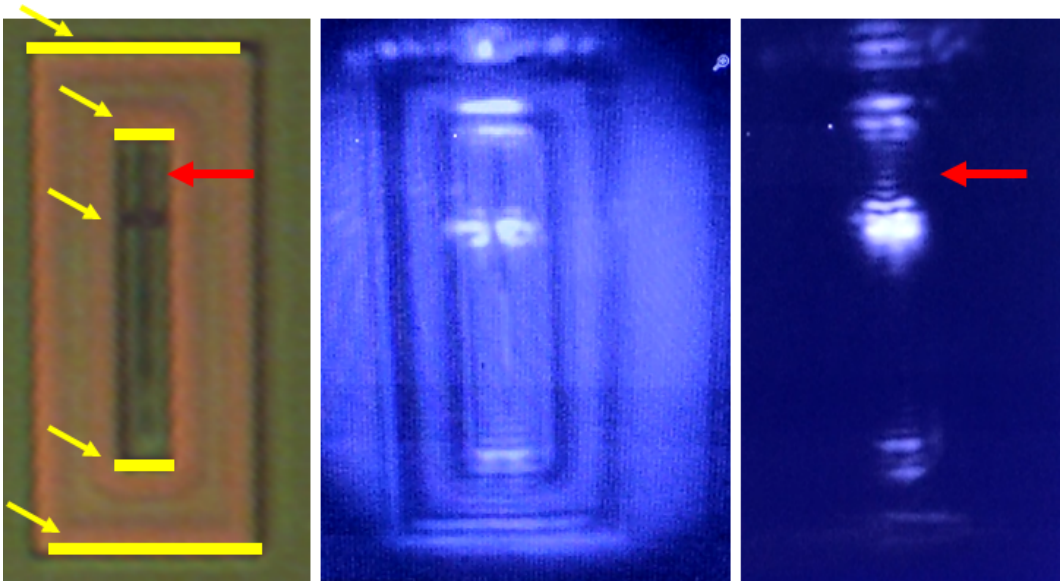

Figure 5.9: Optical image of tapered waveguide and IR images of tapered fiber placed near the waveguide. The left image is an optical image of the waveguide under an optical microscope, with vertical surfaces that can scatter light marked in yellow. Middle and right images are taken in IR with a fiber aligned with the waveguide with the white light source on (middle) and off (right).

Chapter 6

CONCLUSION

In this thesis, we have demonstrated significant progress towards the usage of tapered optical fibers as an efficient interface for coupling light into tapered silicon nanophotonic waveguides. We investigated a series of simulations to model this coupling interface and understand the geometrical requirements for a taper to be an efficient coupler. We then applied these simulations to provide recommended taper geometries that are expected to provide almost perfect transmission ($> 99\%$) into a silicon waveguide. With these geometries in hand as a guide, we experimented with and optimized the wet etching procedure of an optical fiber using HF and buffered HF to achieve a repeatable taper that matched our recommendations from simulations. At the same time, we also fabricated tapered silicon nanophotonic waveguides using electron-beam lithography and demonstrated successful coupling of 1535 nm light from the tapered fiber into the waveguide with a moderately high efficiency of 11.4%. These preliminary results are promising as they are already comparable with the $20 \sim 30\%$ efficiencies achieved in past experiments, and we are confident that this interface can be optimized to achieve the theoretical efficiencies of over 90%. This study therefore demonstrates that tapered fibers do indeed have the potential to boost the efficiencies of future quantum memories and quantum light-matter interfaces using rare-earth ions by acting as a crucial and reliable optical-coupling component.

6.1 Future Directions

At the same time, there are still many areas that could certainly be improved upon, starting with our two primary factors for our lower-than-expected coupling efficiency. The first goal would be to fabricate better silicon photonic crystal mirrors in order to aid the reflection measurements for our testing of the coupling efficiency. By having photonic crystal holes that match the theoretical recommendations, we could potentially obtain up to a $20\times$ boost in the reflected signal. This would help in the detection of weak reflection signals that could indicate that our fiber is slightly misaligned, from which we could find the optimal alignment more efficiently. This goal would require further testing and iterations on the e-beam dose for both the waveguide itself as well as the surrounding border to overcome the proximity effect.

Other possible variables to be optimized for include the holes' dimension biases as well how far from the border the holes are placed, since we suspect that most of the proximity effect arises from the doses to the border. In a different direction, we could consider removing the silicon support beams that are current supporting the waveguide, as they lead to a non-negligible power loss of about 10% from our simulations. Tests would be necessary to determine if their removal leads to any significant increase breakage rates of silicon waveguides during the wet etch process.

There are also several avenues for improving on our other point of difficulty, which is the difficulty in properly aligning the fiber with the waveguide to achieve optimal coupling. Part of the reason is likely due to the fact that the waveguide taper is extremely narrow at the region where most of the light is coupled from the fiber into the waveguide, and thus any transverse shift of the fiber will cause the fiber to miss the waveguide completely and instead couple the light out into the air. In order to circumvent this, it might be possible to consider decreasing the waveguide taper rate or increasing the waveguide minimum width. Of course, additional simulations will be necessary to determine if these changes can be made while still maintaining a high coupling efficiency.

On the other hand, we can also consider improvements in our alignment procedure to make it more systematic and repeatable, since it is currently done purely manually and is time-consuming. One possible method might to be attempt to automate the fiber alignment procedure as our piezoelectric controller has inputs which can be used to automatically adjust the output voltage and thus control the fiber position precisely. A system could then be set up where the piezoelectric stack is set to scan across a grid of positions to map out the position which gives rise to the highest reflected power.

For a somewhat longer-term goal, once we have mastered how to couple efficiently into these free-standing waveguides on an SOI chip, we might wish to start shifting to silicon nanophotonic waveguides deposited on top of YSO or YVO crystals. In order to make this shift, one necessary fabrication problem we would then need to solve is our need to create an air gap below the silicon waveguide through a "bridge" so that we avoid the undesirable coupling directly between the fiber and the underlying crystal. This is somewhat of an unsolved fabrication problem, and would likely involve some local sacrificial layer that the silicon tapered waveguide will be deposited on top of to create the raised bridge structure. Once this is achieved, this would open the door to incorporating these silicon waveguides with photonic

crystal cavities using the mature and well-developed platform of silicon photonics, and can potentially help us realize scalable and highly efficient cavity-coupled ions for quantum information storage as quantum memories and for optical state readout as quantum light-matter interfaces.

BIBLIOGRAPHY

[1] C. Neill et al. "A blueprint for demonstrating quantum supremacy with superconducting qubits". In: *Science* 360.6385 (Apr. 2018), pp. 195–199. DOI: 10.1126/science.aao4309. URL: https://doi.org/10.1126/science.aao4309.

[2] David C. McKay et al. "Efficient Z gates for quantum computing". In: *Physical Review A* 96.2 (Aug. 2017). DOI: 10.1103/physreva.96.022330. URL: https://doi.org/10.1103/physreva.96.022330.

[3] K. Wright et al. *Benchmarking an 11-qubit quantum computer*. 2019. eprint: arXiv:1903.08181.

[4] John Preskill. *Quantum computing and the entanglement frontier*. 2012. eprint: arXiv:1203.5813.

[5] Peter W. Shor. "Polynomial-Time Algorithms for Prime Factorization and Discrete Logarithms on a Quantum Computer". In: *SIAM Journal on Computing* 26.5 (Oct. 1997), pp. 1484–1509. DOI: 10.1137/s0097539795293172. URL: https://doi.org/10.1137/s0097539795293172.

[6] Esteban A. Martinez et al. "Real-time dynamics of lattice gauge theories with a few-qubit quantum computer". In: *Nature* 534.7608 (June 2016), pp. 516–519. DOI: 10.1038/nature18318. URL: https://doi.org/10.1038/nature18318.

[7] P. J. J. O'Malley et al. "Scalable Quantum Simulation of Molecular Energies". In: *Physical Review X* 6.3 (July 2016). DOI: 10.1103/physrevx.6.031007. URL: https://doi.org/10.1103/physrevx.6.031007.

[8] H. J. Kimble. "The quantum internet". In: *Nature* 453.7198 (2008), pp. 1023–1030. DOI: 10.1038/nature07127. URL: https://doi.org/10.1038/nature07127.

[9] Stephan Ritter et al. "An elementary quantum network of single atoms in optical cavities". In: *Nature* 484.7393 (Apr. 2012), pp. 195–200. DOI: 10.1038/nature11023. URL: https://doi.org/10.1038/nature11023.

[10] Nicolas Gisin et al. "Quantum cryptography". In: *Reviews of Modern Physics* 74.1 (Mar. 2002), pp. 145–195. DOI: 10.1103/revmodphys.74.145. URL: https://doi.org/10.1103/revmodphys.74.145.

[11] Charles H. Bennett and Gilles Brassard. "Quantum cryptography: Public key distribution and coin tossing". In: *Theoretical Computer Science* 560 (Dec. 2014), pp. 7–11. DOI: 10.1016/j.tcs.2014.05.025. URL: https://doi.org/10.1016/j.tcs.2014.05.025.

[12] Dimitris Giampouris. “Short Review on Quantum Key Distribution Protocols”. In: *Advances in Experimental Medicine and Biology*. Springer International Publishing, 2017, pp. 149–157. DOI: 10.1007/978-3-319-56246-9_12. URL: https://doi.org/10.1007/978-3-319-56246-9_12.

[13] *Corning SMF-28e+ Optical Fiber*. PI1463. Corning. July 2014.

[14] H.-J. Briegel et al. “Quantum Repeaters: The Role of Imperfect Local Operations in Quantum Communication”. In: *Physical Review Letters* 81.26 (Dec. 1998), pp. 5932–5935. DOI: 10.1103/physrevlett.81.5932. URL: https://doi.org/10.1103/physrevlett.81.5932.

[15] David D. Awschalom et al. “Quantum technologies with optically interfaced solid-state spins”. In: *Nature Photonics* 12.9 (Aug. 2018), pp. 516–527. DOI: 10.1038/s41566-018-0232-2. URL: https://doi.org/10.1038/s41566-018-0232-2.

[16] K. Heshami et al. “Quantum memories: emerging applications and recent advances”. In: *Journal of Modern Optics* 63.20 (2016), pp. 2005–2028. DOI: 10.1080/09500340.2016.1148212. URL: https://doi.org/10.1080/09500340.2016.1148212.

[17] Aleks K. Rebane et al. “Maximum coherence in optical transitions in rare-earth-ionactivated solids”. In: *Advances in Photonics of Quantum Computing, Memory, and Communication III*. Ed. by Zameer U. Hasan et al. SPIE, Feb. 2010. DOI: 10.1117/12.848879. URL: https://doi.org/10.1117/12.848879.

[18] M. Zhong et al. “Optically addressable nuclear spins in a solid with a six-hour coherence time”. In: *Nature* 517.7533 (2015), pp. 177–180. DOI: 10.1038/nature14025. URL: https://doi.org/10.1038/nature14025.

[19] Miloš Rančić et al. “Coherence time of over a second in a telecom-compatible quantum memory storage material”. In: *Nature Physics* 14.1 (Sept. 2017), pp. 50–54. DOI: 10.1038/nphys4254. URL: https://doi.org/10.1038/nphys4254.

[20] Anatole Abragam and B. Bleaney. *Electron Paramagnetic Resonance of Transition Ions*. London: Oxford University Press, 1970. ISBN: 0198512503.

[21] Xavier Fernandez-Gonzalvo et al. “Coherent frequency up-conversion of microwaves to the optical telecommunications band in an Er:YSO crystal”. In: *Physical Review A* 92.6 (Dec. 2015). DOI: 10.1103/physreva.92.062313. URL: https://doi.org/10.1103/physreva.92.062313.

[22] Jonathan Miners Kindem. “Quantum nanophotonics with ytterbium in yttrium orthovanadate”. PhD thesis. Pasadena, California: California Institute of Technology, Mar. 2019.

[23] E. M. Purcell. “Spontaneous Emission Probabilities at Radio Frequencies”. In: *Confined Electrons and Photons*. Springer US, 1995, pp. 839–839. DOI: 10.1007/978-1-4615-1963-8_40. URL: https://doi.org/10.1007/978-1-4615-1963-8_40.

[24] Tian Zhong et al. “Nanophotonic coherent light–matter interfaces based on rare-earth-doped crystals”. In: *Nature Communications* 6.1 (2015). DOI: 10.1038/ncomms9206. URL: https://doi.org/10.1038/ncomms9206.

[25] Tian Zhong et al. “Nanophotonic rare-earth quantum memory with optically controlled retrieval”. In: *Science* 357.6358 (2017), pp. 1392–1395. DOI: 10.1126/science.aan5959. URL: https://doi.org/10.1126/science.aan5959.

[26] Evan Miyazono et al. “Coupling erbium dopants in yttrium orthosilicate to silicon photonic resonators and waveguides”. In: *Optics Express* 25.3 (2017), p. 2863. DOI: 10.1364/oe.25.002863. URL: https://doi.org/10.1364/oe.25.002863.

[27] Tian Zhong et al. “Optically Addressing Single Rare-Earth Ions in a Nanophotonic Cavity”. In: *Physical Review Letters* 121.18 (Oct. 2018). DOI: 10.1103/physrevlett.121.183603. URL: https://doi.org/10.1103/physrevlett.121.183603.

[28] Evan Tsugio Miyazono. “Nanophotonic Resonators for Optical Quantum Memories Based on Rare-Earth-Doped Materials”. PhD thesis. Pasadena, California: California Institute of Technology, Apr. 2017.

[29] Tian Zhong et al. “High quality factor nanophotonic resonators in bulk rare-earth doped crystals”. In: *Optics Express* 24.1 (2016), p. 536. DOI: 10.1364/oe.24.000536. URL: https://doi.org/10.1364/oe.24.000536.

[30] Riccardo Marchetti et al. “High-efficiency grating-couplers: demonstration of a new design strategy”. In: *Scientific Reports* 7.1 (2017). DOI: 10.1038/s41598-017-16505-z. URL: https://doi.org/10.1038/s41598-017-16505-z.

[31] Justin D. Cohen, Seán M. Meenehan, and Oskar Painter. “Optical coupling to nanoscale optomechanical cavities for near quantum-limited motion transduction”. In: *Optics Express* 21.9 (2013), p. 11227. DOI: 10.1364/oe.21.011227. URL: https://doi.org/10.1364/oe.21.011227.

[32] Simon Gröblacher et al. “Highly efficient coupling from an optical fiber to a nanoscale silicon optomechanical cavity”. In: *Applied Physics Letters* 103.18 (2013), p. 181104. DOI: 10.1063/1.4826924. URL: https://doi.org/10.1063/1.4826924.

[33] T. G. Tiecke et al. “Efficient fiber-optical interface for nanophotonic devices”. In: *Optica* 2.2 (2015), p. 70. DOI: 10.1364/optica.2.000070. URL: https://doi.org/10.1364/optica.2.000070.

[34] Xia Chen, Chao Li, and Hon K. Tsang. "Device engineering for silicon photonics". In: *NPG Asia Materials* 3.1 (2011), pp. 34–40. DOI: 10.1038/asiamat.2010.194. URL: https://doi.org/10.1038/asiamat.2010.194.

[35] Michael J. Burek et al. "Fiber-Coupled Diamond Quantum Nanophotonic Interface". In: *Physical Review Applied* 8.2 (2017). DOI: 10.1103/physrevapplied.8.024026. URL: https://doi.org/10.1103/physrevapplied.8.024026.

[36] Dennis R. Turner. *Etch Procedure for Optical Fibers*. U.S. Patent 4,469,554. 1984.

[37] John D. Joannopoulos et al. *Photonic Crystals: Molding the Flow of Light*. Princeton: Princeton University Press, 2008. ISBN: 978-0-691-12456-8.

[38] *Wave Optics Module User's Guide*. Version 4.3b. COMSOL. May 2013.

[39] J.D. Love et al. "Tapered single-mode fibres and devices. Part 1: Adiabaticity criteria". In: *IEE Proceedings J Optoelectronics* 138.5 (1991), p. 343. DOI: 10.1049/ip-j.1991.0060. URL: https://doi.org/10.1049/ip-j.1991.0060.

[40] Sophocles J. Orfanidis. *Electromagnetic Waves and Antennas*. Rutgers University, Aug. 2016. URL: https://www.ece.rutgers.edu/~orfanidi/ewa/ewa-2up.pdf.

[41] G. A. Valaskovic, M. Holton, and G. H. Morrison. "Parameter control, characterization, and optimization in the fabrication of optical fiber near-field probes". In: *Applied Optics* 34.7 (Mar. 1995), p. 1215. DOI: 10.1364/ao.34.001215. URL: https://doi.org/10.1364/ao.34.001215.

[42] J. M. Ward et al. "Contributed Review: Optical micro- and nanofiber pulling rig". In: *Review of Scientific Instruments* 85.11 (Nov. 2014), p. 111501. DOI: 10.1063/1.4901098. URL: https://doi.org/10.1063/1.4901098.

[43] Wooyoung Han. "Nanoscale Fiber Tip Probe for Biomedical and Intracellular Sensing". PhD thesis. Cambridge, Massachusetts: Harvard University, Graduate School of Arts and Sciences, June 2016.

[44] Patrik Hoffmann, Bertrand Dutoit, and René-Paul Salathé. "Comparison of mechanically drawn and protection layer chemically etched optical fiber tips". In: *Ultramicroscopy* 61.1-4 (Dec. 1995), pp. 165–170. DOI: 10.1016/0304-3991(95)00122-0. URL: https://doi.org/10.1016/0304-3991(95)00122-0.

[45] L. H. Haber et al. "Shape control of near-field probes using dynamic meniscus etching". In: *Journal of Microscopy* 214.1 (2004), pp. 27–35. DOI: 10.1111/j.0022-2720.2004.01308.x. URL: https://doi.org/10.1111/j.0022-2720.2004.01308.x.

[46] COMSOL AB. *COMSOL Multiphysics v. 5.3a.* Version 5.3a. Dec. 14, 2017. URL: https://www.comsol.com.

[47] *Cyantek Corporation Safety Data Sheet Nano-Strip, Nano-Strip HP*. MSDS 17-139. Cyantek Corporation. June 2013.

[48] *Beamer: Electron- and Laser-Beam Lithography Software*. GenISys. 2017. URL: https://genisys-gmbh.com/assets/downloadInfos/Beamer_2017_web.pdf.

[49] Michael David Henry. "ICP Etching of Silicon for Micro and Nanoscale Devices". PhD thesis. Pasadena, California: California Institute of Technology, May 2010.

[50] Eunsung Seo, Bo Kyung Choi, and Ohyun Kim. "Determination of proximity effect parameters and the shape bias parameter in electron beam lithography". In: *Microelectronic Engineering* 53.1-4 (June 2000), pp. 305–308. DOI: 10.1016/s0167-9317(00)00320-8. URL: https://doi.org/10.1016/s0167-9317(00)00320-8.